EXPERIMENTS ON TURBULENCE FROM COLLIDING ICE FLOES

Trygve K. Løken[1,*], Aleksey Marchenko[2], Thea J. Ellevold[3], Jean Rabault[4] and Atle Jensen[3]

May 25, 2022

[1] Department of Mathematics Teaching and Learning, Nord University, Bodø, Norway
[2] Department of Arctic Technology, The University Centre in Svalbard, Longyearbyen, Norway
[3] Department of Mathematics, University of Oslo, Oslo, Norway
[4] Information Technology Department, Norwegian Meteorological Institute, Oslo, Norway

ABSTRACT

Increased knowledge about energy dissipation processes around colliding ice floes is important for improved understanding of atmosphere-ice-ocean energy transfer, wave propagation through sea ice and the polar climates. The aim of this study is to obtain such information by investigating colliding ice floe dynamics in a large-scale experiment and directly measuring and quantifying the turbulent kinetic energy (TKE). The field work was carried out at Van Mijen Fjord on Svalbard, where a 3×4 m ice floe was sawed out in the fast ice. Ice floe collisions and relative water-ice motion was generated by pulling the ice floe back and forth in an oscillatory manner in a 4×6 m pool, using two electrical winches. Ice floe motion was measured with a range meter and accelerometers, and the water turbulence was measured acoustically with Doppler velocimeters and optically with a remotely operated vehicle and bubbles as tracers. Turbulent kinetic energy spectra were found to contain an inertial subrange where energy was cascading at a rate proportional to the -5/3 power law. The TKE dissipation rate was found to decrease exponentially with depth. The total TKE dissipation rate was estimated by assuming that turbulence was induced over an area corresponding to the surface of the floe. The results suggest that approximately 37% and 8% of the input power from the winches was dissipated in turbulence and absorbed in the collisions, respectively, which experimentally confirms that energy dissipation by induced turbulent water motion is an important mechanism for colliding ice floe fields.

[1] Author to whom correspondence should be addressed: trygve.loken@gmail.com

1 Introduction

A decline in the Arctic ice cover has been observed over the past decades (Feltham 2015), which has allowed for more human activities in the region, such as shipping, tourism and exploitation of natural resources (Smith & Stephenson 2013). Better predictions of sea ice hazards are necessary to ensure safe operations in the Marginal Ice Zone (MIZ). The MIZ is the transition between the land fast ice or dense pack ice and the open ocean, which consists of a distribution of discrete ice floes at various concentrations, with dimensions varying from meters to hundreds of meters in length and tens of centimeters to meters in depth (Rottier 1992). On the one hand, the retreating ice cover leads to larger areas of open water in the Arctic where more energetic waves are generated due to the increased fetch, which in turn enhance ice break up processes (Thomson & Rogers 2014). On the other hand, experimental and theoretical studies have shown that waves are exponentially damped in the MIZ (Weber 1987, Wadhams et al. 1988), meaning that the presence of the MIZ mitigates ice cover break up. This interplay illustrates that wave-ice interactions, which are coupled in a nonlinear manner, are key mechanisms for the Arctic. There is uncertainty associated with the dominating source of wave energy dissipation by sea ice, which depends on both the wave and the ice conditions (Shen 2019). Increased knowledge about these physical processes, and hence atmosphere-wave-ice-ocean energy transfer, may improve sea ice dynamics models used for wave forecasts and climate modeling.

Several phenomena are known to attenuate waves in an ice floe field, such as wave scattering or directional spreading and viscous dissipation in the boundary layer below the ice due to shear flow or wake formation caused by a relative velocity between the water and the ice (Wadhams 1975, Liu & Mollo-Christensen 1988, Herman 2021). Scattering, which contributes to wave decay due to energy reflection and spreading, is known to be of importance in open floe fields where the floe diameter is of the same order as the ocean wavelength (Squire et al. 1995). Ice floe interactions can lead to wave energy dissipation through different mechanisms and are of relevance in denser floe fields. Several theoretical models that attempt to describe ice floe motion in periodic wave fields, assume that floes follow the wave orbital velocities at the free surface (Rottier 1992), with the gravity force pulling them down the sloped wave surface (Shen & Ackley 1991). As a result, ice floes respond in surge when acted upon by wave trains entering the MIZ, and periodically recurring collisions between adjacent floes may occur if the floes are sufficiently close since they are moving out of phase with each other (Shen & Ackley 1991, Rottier 1992, Squire et al. 1995). Collisions between neighboring ice floes can, for example, cause momentum transfer and energy absorption during the impulse (Shen & Squire 1998, Herman 2018, Li & Lubbad 2018, Herman et al. 2019). Rabault et al. (2019) showed from wave tank experiments that colliding chunks of grease ice can generate turbulence that injects eddy viscosity in the water, which leads to enhanced energy dissipation. However, scaling problems in, for example, Reynolds number, size ratios and frequency ratios are inevitable in laboratory experiments, which raises the need for performing full-scale measurements outside of the laboratory (see e.g., Rabault et al. (2019) for a discussion on the topic). It would be challenging to reproduce a full-scale ice floe and preserve the size ratio with respect to the ice thickness in a laboratory. For example, in HSVA (Hamburg Ship Model Basin), the ice thickness is usually up to a few 10s of cm (Marchenko et al. 2021).

Mathematical models have been developed to describe wave attenuation in the MIZ, e.g., the viscoelastic model of Zhao & Shen (2018) and the viscous models of Sutherland et al. (2019) and Marchenko et al. (2019a). Sutherland et al. (2019) leave freedom of interpretation of the effective viscosity while Marchenko et al. (2019a) associate the effective viscosity with the eddy viscosity. These models rely on physical parameters, e.g., the effective viscosity, that may be adjusted through curve-fitting exercises to match experimental data, although they may lack direct proof of which phenomena that are of importance. By contrast, direct observations on the full scale can describe in detail the dissipative mechanisms occurring. There are few in situ observations of the water kinematics around interacting ice floes because the harsh conditions make field work challenging, and there is a need for more observations (Shen 2019). Voermans et al. (2019) managed to measure under-ice turbulence in pancake and frazil ice generated from the relative velocity between the ice and the orbital wave motion and suggested that turbulence-induced wave attenuation was similar to total wave attenuation. This means that the influence of floe-floe collisions on wave attenuation was very small in the experiments of Voermans et al. (2019), although they did not directly discuss this mechanism. Marchenko et al. (2015) measured turbulence under continuous drift ice and found that the main source of under-ice turbulence was associated with water motion relative to the ice caused by tidal current and wind drift of the ice. However, the effect of turbulent dissipation around larger interacting ice floes, typically found in the Greenland Sea and Arctic MIZ, has not been previously confirmed experimentally.

In this study, direct observations of the turbulent kinetic energy (TKE) dissipation rate in the immediate vicinity of a colliding full-scale ice floe are presented for the first time. A high level of control over the floe motion and the surrounding water velocity was obtained from an extensive instrumentation, which would have been extremely challenging to deploy in the dynamic and hazardous environment of the MIZ. Hence, an outdoor laboratory on an ice-covered fjord was installed as a compromise between realistic scale and high level of control. An ice floe was cut out from the land fast ice. The ice floe was towed back and forth to generate relative water-ice flow and collisions with the fast ice. The experimental setup was similar to that of Marchenko et al. (2021a), who measured turbulent properties with an acoustic Doppler velocimeter (ADV). The novelty of the current experiment is the use of an acoustic Doppler current profiler (ADCP), which enabled the authors to estimate the TKE dissipation rate on several locations to quantify the importance of turbulence induced from collisions and shear flow, and the use of a remotely operated vehicle (ROV) which, together with a bubble seeding system, allowed the authors to observe 2D water kinematics under the ice. As the ice floe approached the fast ice, fluid was expelled as a planar jet from the closing orifice into the quiescent fluid below the ice, causing free shear turbulence due to the velocity shear between the entering and ambient fluids (Layek & Sunita 2018, Cafiero & Vassilicos 2019, Arote et al. 2020). Large-scale vortex structures in a plane jet cause momentum transfer into the ambient fluid (Breda & Buxton 2018, Takahashi et al. 2019). Energy dissipated in collisions was determined from high resolution accelerometer data. The extensive instrumentation allowed for control of input energy rates and thus estimates of a floe energy balance.

The paper is organized in the following manner. Experimental setup, data acquisition and processing methods are described in Sec. 2. Section 3 contains a mathematical description of the problem. The results in Sec. 4 are presented as

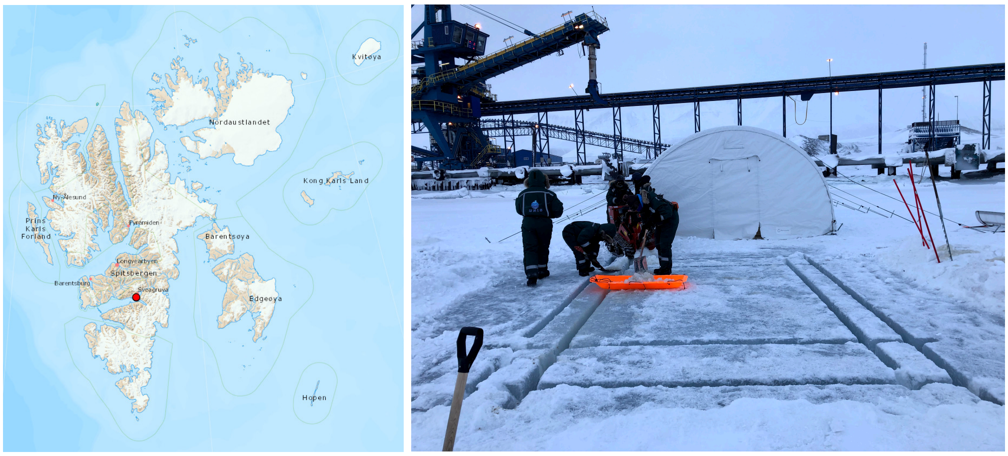

(a) Map indicating experimental site.

(b) Preparation of field laboratory.

Figure 1: Location and preparation of the field laboratory. a) A map of the Svalbard archipelago (red dot indicates the location of the experimental work). Source: TopoSvalbard (2021). b) The working process of cutting the ice. The frame between the outer and inner rectangle was removed to create a floating ice floe in a pool. Afterwards, the inflatable tent in the background was placed over the pool for weather protection.

an energy budget where the rate of energy input is compared with the rate of dissipation. Finally, a discussion on the accuracy and implications of the results follows in Sec. 5, and the concluding remarks are given in Sec. 6.

2 Data and methods

The field work was carried out next to the harbor in the Svea Bay on Svalbard on March 3-12, 2020. The location is indicated with a red dot in Fig. 1a and the geographical coordinates were 77.86°N, 16.65°E. Svea Bay is part of the Van Mijen Fjord which was covered with land fast ice at the time of the field campaign (see Marchenko et al. (2021b) for details on ice properties). An ice floe was made at the selected site where the ice thickness was approximately 1 m. Figure 1b shows an outer and an inner rectangle measuring 6×4 m and 4×3 m, respectively, which were cut through the sea ice by means of a walk-behind chain trencher and hand saws. The ice between the two rectangles were broken into manageable blocks and removed with chains and hoists installed on a quadpod lifting rig, resulting in a floating ice floe in a pool. A 10×6 m inflatable tent was placed over the pool for weather protection and equipped as a field laboratory.

A coordinate system, shown in Fig. 2, was defined with the (x, y, z)-axis to be aligned horizontally in the axial and transverse direction of the pool and vertically in upward direction, respectively. The coordinate system is consistent throughout the text. The x-axis was oriented with an angle $\alpha = 28°$ counterclockwise from the magnetic north. Hence, the short ends of the pool were defined as the north and south ends. The origin was defined as $x = 0$ at the pool south end, $y = 0$ at the pool center and $z = 0$ at the bottom of the ice. The coordinate system included in Fig. 2a is displaced along the z-axis to the top side of the ice for increased readability. The floe dimensions L_f, W_f and H_f in the x, y and z-directions were 4, 3 and 1 m, respectively.

Experiment	Cycles [N]		ADCP		Load cell
	Total	ADV	Cells [N]	Position	
1	15	15	95	1	-
2	14	14	39	1	-
3	11	5	95	1	✓
4	28	20	39	2	-
5	7	5	39	2	-
6	8	-	39	3	-

Table 1: Experimental details and instrument settings. The different ADCP positions are indicated in Fig. 2b.

At the location of the field laboratory, there was negligible wave energy. Therefore, two electrical winches were used to tow the ice floe back and forth in an oscillatory manner in the x-direction to generate relative water-ice motion and collisions with the fast ice. One period of oscillation, i.e., the floe motion back and forth, will be referred to as a *cycle*. The winches were mounted to the fast ice by means of ice screws, one on each short end, approximately 3 m from the pool at $y = 0$. A wooden frame was attached to the floe with ice screws and the winch wires were coupled to the frame via a polyester silk rope as illustrated in Fig. 2a to distribute the winch load over a large area of the floe surface. The winches were alternating in pulling and slacking and were manually actuated by two persons.

2.1 Instrumentation

Six experiments, summarized in Table 1, are included in this paper. The only variables that were changed between the experiments were the number of cycles, the position and cell configuration of the ADCP and the inclusion of a load cell and accelerometers. All other parameters, such as the towing speed and the duration of the cycles, were kept approximately constant in all the experiments. The similar setup was used several times to investigate the repeatability of the experiments.

Several sensors and instruments were installed on the south end of the pool, as shown in Fig. 2, to measure the ice floe and water motion. An evo60 LED (light-emitting diode) range meter was pointing towards a large box placed on the floe, which provided time series of the floe surge, i.e., displacement in the x-direction. The sample frequency of the range meter was approximately 125 Hz and the raw data were smoothed with a moving average over 200 data points. The computer that was used to control the range meter was synchronized with Internet time each day. The ice floe velocity in the x-direction was found from the smoothed position with a central difference scheme. An example of a time series from the range meter, where the floe undergoes 11 full cycles, is displayed in the upper panel of Fig. 3. The floe was displaced approximately 1.7 m and the maximum towing velocity V_{max} was constant and about 0.15 m/s in each direction. The oscillating period in ice floe surge T_s, i.e., the duration of one cycle, was around 26 s.

During Exp. 3, a load cell (PCM BD-ST-620) was mounted in the coupling between the winch wire and the polyester silk rope. Only one load cell was available, and it was installed at the south end of the pool, which means that it measured towing force applied by the winch on the ice floe in the $-x$-direction. In the same experiment, two uniaxial

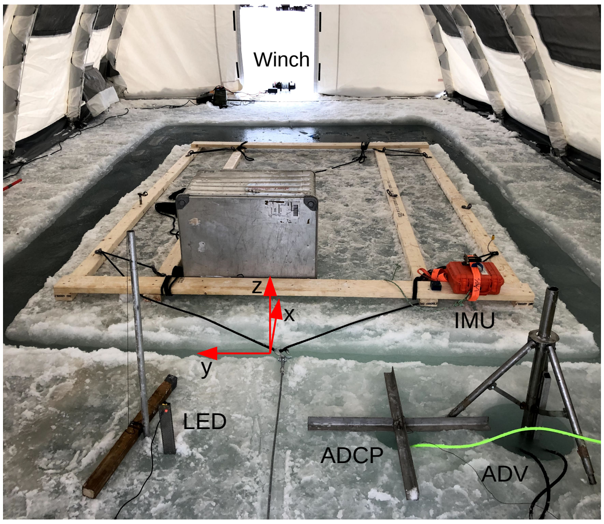

(a) Seen from the south end of the pool.

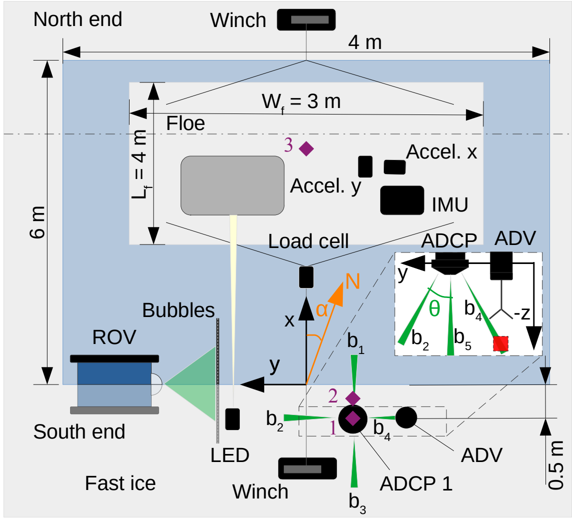

(b) Seen from above.

Figure 2: Experimental setup. a) Photo of the setup seen from the south end of the pool. The defined coordinate system is indicated (although displaced from the origin along the z-axis to the top side of the ice for the illustrative purpose). The load cell and the uniaxial accelerometers were not installed during this particular experiment. b) Schematic of the setup in the xy-plane, where the dot-dashed line indicates image compression in the longitudinal direction. Magnetic north (N) is indicated. The various positions of the ADCP are indicated with purple diamonds and are labeled with numbers, where the distance from the pool edge to Position 1 and 2 are 0.50 and 0.25 m, respectively, and Position 3 is the center of the ice floe. The inset sketch shows the acoustic instruments in the yz-plane and the measurement volume of the ADV is marked with a red square, which coincides with a part of the ADCP $\mathbf{b_4}$.

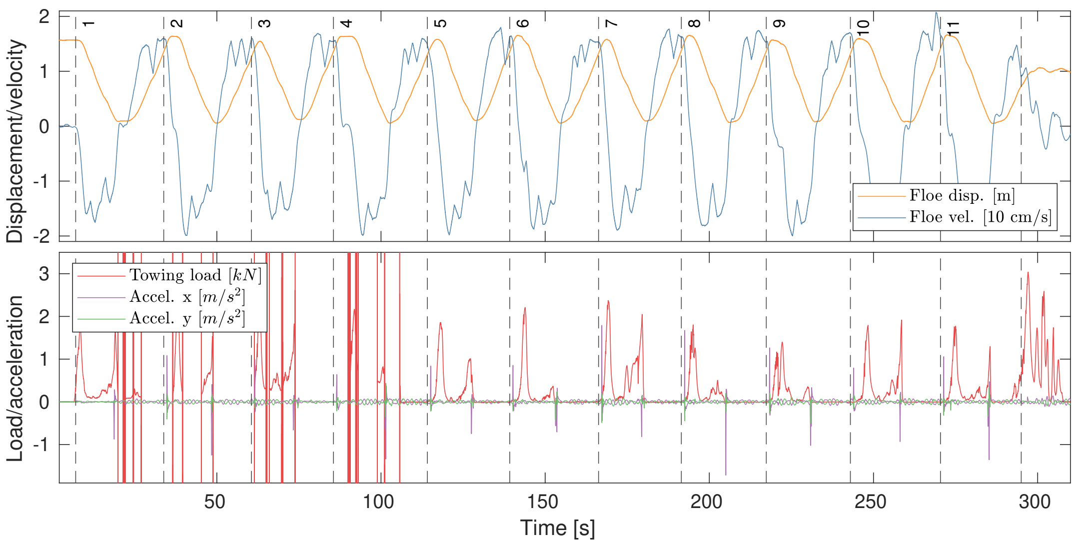

Figure 3: Time series from Exp. 3 where the cycles are marked with numbers and separated with vertical dashed lines. Upper panel: range meter data with smoothed displacement and velocity of the ice floe in the x-direction. Lower panel: load cell and uniaxial accelerometers. Note that Cycles 2-4 contain severe load cell dropouts.

Instrument	Sample freq. [Hz]	Moving avg. [N]	Synchronization	Common freq. [Hz]
Range meter	125	200	♦	1000
Load cell	5000	500	♦	1000
Accelerometer	5000	500	♦	1000
IMU	10	-	♦	-
ADCP	8	10	★	80
ADV	10	10	★	80
ROV	30	-	-	-

Table 2: Instrument configurations and synchronization. The range meter, IMU, ADCP and ROV were synchronized with Internet time each day. The symbols indicate the instruments that were synchronized in time in the post-processing.

accelerometers (Bruel and Kjær, DeltaTron Type 8344) suitable for collision measurements, were mounted on the floe, one aligned with the $-x$-direction and the other with the y-direction, as seen in Fig. 2b. The sampling frequency of the load cell and the accelerometers was 5 kHz and the signals were smoothed with a Savitzky-Golay filter over 500 data points. An example of a time series from the load cell and the uniaxial accelerometers is displayed in the lower panel of Fig. 3, where the accelerometer data contain two high-amplitude events per cycle, corresponding to collision with the fast ice, and low-amplitude oscillations with a period around 2 s in between, possibly associated with surface waves in the pool. The load cell and the two accelerometers were connected to the same data acquisition unit and were therefore synchronized. However, the computer used to control the instruments was not synchronized with Internet time. In the post-processing, it was necessary to synchronize the range meter and load cell data in time, as there was a mismatch between the computer clocks. Table 2 lists the instruments that were synchronized in the post-processing, their sampling frequencies and smoothing parameters. Details on the synchronization scheme for the instruments marked with diamonds in Table 2 can be found in Appendix A.

Ice floe motion was also measured with a VN-100 IMU (inertial motion unit) manufactured by VectorNav. The instrument was installed in a rugged box with batteries and a processing unit, see Rabault et al. (2020) for details. The IMU contained a three-axis accelerometer, gyroscope and magnetometer, and allowed for surveillance of all six rigid body motion modes. An integrated GPS tracker provided correct GPS timestamps to the measurements. The sampling frequency was 10 Hz. By examination of the IMU data, it was found that surge was the predominant rigid body motion mode of the ice floe. This is not surprising since the towing was performed in this direction. Some motion was also observed in the other horizontal modes, sway and yaw, i.e., translation in the y-direction and rotation about the z-axis, respectively, as the floe did not move perfectly parallel to the pool walls. The motion in the vertical modes, heave, roll and pitch, was found to be negligible in comparison with the horizontal motion. The surge and heave motions are compared in Fig. 15 in Appendix B.

A five beam Nortek Signature1000 (kHz) broadband ADCP was utilized to measure the water velocity in the vicinity of the ice floe. The instrument was operated in the pulse coherent mode, also known as the *high-resolution mode* that enables very small cell size on all beams, which is desirable for turbulence measurements. It was mounted downward-facing through a hole in the fast ice from a specially constructed frame, so that the transducer head was 3 cm below the bottom of the ice (i.e., at $z = -3$ cm). The x-position was either -0.50 m or -0.25 m and the y-position was -0.50 m. In Exp. 6, the ADCP was placed on the ice floe center. The instrument has one vertically oriented beam $\mathbf{b_5}$, which was pointing in the $-z$-direction, and four slanted beams $\mathbf{b_1} - \mathbf{b_4}$ diverging at $\theta = 25°$ from the vertical. The horizontal components of $\mathbf{b_1} - \mathbf{b_4}$ were pointing in the x, y, $-x$ and $-y$- direction, respectively, as seen in Fig. 2b. Water velocity along the five beam directions (positive direction was radially away from the instrument) is denoted b_j for $j = 1, 2, ..., 5$.

The mean horizontal velocity components due to the tidal current (measured when the floe was not moving) $\langle u \rangle$ and $\langle v \rangle$, corresponding to x and y-directions, respectively, were calculated as $\langle u \rangle = \langle b_1 \sin(\theta) - b_3 \sin(\theta) \rangle$ and $\langle v \rangle = \langle b_2 \sin(\theta) - b_4 \sin(\theta) \rangle$, where the angle brackets denote time averaging over the duration of the time series. The mean horizontal current speed U_{mean} was calculated as $U_{mean} = \sqrt{\langle u \rangle^2 + \langle v \rangle^2}$. The ADCP measurement rate was 8 Hz, which is the maximum possible sampling frequency when all the beams are operated. A blanking distance of 10 cm was applied to avoid transducer ringing. The profiling range was 1.9 m and the bin size was either 2 or 5 cm, which yielded 95 or 39 bins, respectively. The instrument settings and placement are summarized in Table 1.

In order to validate the data from the current profiler, a 5 MHz SonTek Hydra ADV was deployed next to the ADCP. The instrument was mounted through a second hole in the fast ice with the measurement volume centered 58 cm below the bottom of the ice (i.e., at $z = -58$ cm). The two acoustic instruments were situated in the same x-position and the y-position of the ADV was carefully selected so that its measurement volume was very close to the ADCP $\mathbf{b_4}$, as illustrated in Fig. 2b. The short distance between the two instruments was possible due to the different acoustic frequencies. The ADV was configured with a fixed measurement interval with 10 min continuous sampling followed by 1.67 min down-time. Consequently, not all the cycles were sampled if the instrument down-time coincided with the experiment. Table 1 lists the total amount of cycles and cycles sampled by the ADV in the experiments. The ADV measurement frequency was 10 Hz. It was configured to output ENU (east, north and up) velocity components, which were converted to u and v-components corresponding to x and y-directions, respectively, according to $u = N \cos(\alpha) - E \sin(\alpha)$ and $v = -N \sin(\alpha) - E \cos(\alpha)$. The w-component corresponding to the z-direction was simply $w = U$. The ADV velocity component vw corresponding to the ADCP b_4 velocity was calculated as $vw = -v \sin(\theta) - w \cos(\theta)$, which enabled a direct comparison of the time series from the two instruments on the location indicated by the red square in Fig. 2b.

In the post-processing, the ADCP and ADV data were re-sampled to a common sampling rate of 80 Hz and synchronized in time with a cross-correlation optimization method (marked with stars in Table 2), see Løken et al. (2021b) for further details. An example of a time series from the acoustic Doppler instruments is shown in Fig. 4, where the ADCP b_4 from the bin closest to the ADV measurement volume and the ADV vw are presented. The instruments agree on the larger turbulent scales, but there are some discrepancies, especially on the smaller scales. The two presented time series were recorded spatially very close to each other, but there is of course a limit to how accurately instruments can be placed in field experiments, and there may have been small variations in the ice thickness which led to small errors in

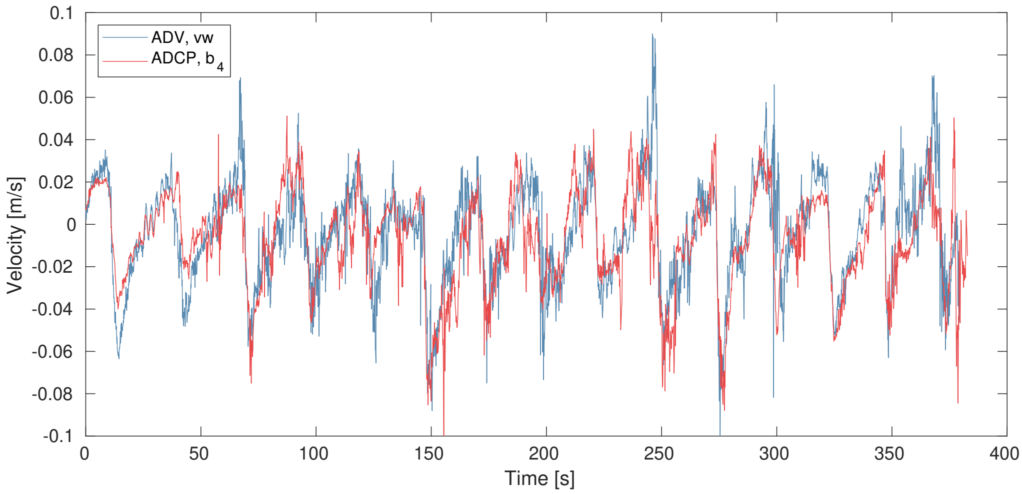

Figure 4: Time series from acoustic Doppler instruments in Exp. 1. The ADCP b_4 is from the bin which is located at the same z-position as the ADV measurement volume. The ADV vw is the velocity component corresponding to the along-beam velocity of the ADCP $\mathbf{b_4}$. The two measurement volumes were placed as close to each other as possible.

the estimated position. In addition, the measurement volumes are different for the ADV and the ADCP, in the order of 1 and 100 cm^3, respectively. The large-scale fluctuations indicate that the ice floe undergoes 15 full cycles.

In addition to acoustic measurements, fluid motion was also visualized with bubbles as tracing particles. Bubbles were generated from a thin, 0.5 m long carbon fiber pipe perforated every 1 cm on the upward facing side with a 0.1 mm drill bit. The pipe was fed with air of approximately 0.4 bar from a compressor, via a 5 m long flexible rubber hose. This configuration provided an array of bubbles with approximately 2-3 mm diameter. The bubble pipe was attached to the bottom of a metal grid, which was suspended below the ice from strings of thin rope. The bubble pipe was hanging horizontally, aligned with the x-axis at $z \approx -1$ m. Bubble motion was recorded with the camera of a BlueROV2 (BlueRobotics 2020) remotely operated vehicle, which was steered below the ice with the camera axis perpendicular to the bubble plane. The frame rate was 30 frames/s and other camera settings such as exposure, brightness and gain were adjusted to ensure that the bubbles appeared as clear, circular particles. The setup, which is illustrated in Fig. 2b, is further described and validated in Løken et al. (2021a).

2.2 Turbulence analysis

Beam correlation is a quality indicator for acoustic velocimeters, which should exceed 50% for the ADCP and 70% for the ADV per manufacturer recommendation. Some spikes occurred in the time series, typically where the correlation dropped below the recommended values. Spikes were identified as velocities outside a range of the moving mean velocity, which was calculated over a sliding window of 10 data points (Marchenko et al. 2021a), ± 3 times the standard deviation (Nystrom et al. 2007). For the spectral analysis, which requires continuous time series, the identified spikes were cut where they exceeded the moving mean velocity ± 3 times the standard deviation. In calculations of statistical parameters, such as variance, the spikes were discarded. The fluctuating velocity component in any direction $u_i' = u_i - \langle u_i \rangle$, where $\langle u_i \rangle$ is the time average over the whole time series, was used in the turbulence analysis. For the comparison of turbulent properties obtained from the ADCP and the ADV, time series containing the same number of cycles were used in the analysis, even though the ADCP sampled all the cycles in the experiments (see Table 1).

Turbulent kinetic energy frequency spectra, also known as power spectral densities $PSD_w(f)$, where f is the frequency, were estimated from the vertical fluctuating velocity component w' with the Welch method (Earle 1996), which means fast Fourier transformation and ensemble averaging of overlapping segments. Each time series was divided into 50 s segments with 50% overlap and a Hamming window was applied to each segment to reduce spectral leakage. Depending on the number of cycles recorded in each experiment (5-20), the resulting spectra had approximately 6-28 degrees of freedom. The TKE frequency spectra represent the distribution of turbulent kinetic energy over the frequencies $0 < f < f_N$, where f_N is the Nyquist frequency, which was 4 and 5 Hz for the ADCP and the ADV, respectively.

Acoustic instruments have intrinsic Doppler noise n in the beam velocity measurements, which is caused when the Doppler shift is estimated from finite-length pulses (Voulgaris & Trowbridge 1998). The Doppler noise often results in flat TKE frequency spectra, also known as the noise floor, typically towards the higher frequencies where the turbulent energy is low. From inspections of both ADCP and ADV data, it was observed that the noise floor was reached close to the Nyquist frequency. Therefore, the noise floor was found by averaging the 20 highest frequencies of the TKE spectra, which corresponds to frequencies in the range 3.7-4 and 4.6-5 Hz for the ADCP and the ADV, respectively. Following Thomson et al. (2012), the noise variance n^2 was estimated by integrating the noise floor over the range of frequencies $0 < f < f_N$, assuming white noise spectra. The Doppler noise can vary with flow speed and distance from the transducer, so the ADCP noise variance was therefore estimated for all beams and bins.

The velocity variance $\langle u_i'^2 \rangle$ was obtained by squaring and time averaging the fluctuating velocity components. The Doppler noise was removed from the velocity variance statistically (Lu & Lueck 1999) by subtracting the noise variance, so that $\langle u_i'^2 \rangle = var(u_i') - n^2$. Instances that were considered to be spikes or with correlation less than the recommended values were removed from the time series before the calculations of the velocity variance were made. Following Dewey & Stringer (2007), the total TKE density TK was calculated as

$$TK_{ADV} = \rho_w \frac{\langle u'^2 \rangle + \langle v'^2 \rangle + \langle w'^2 \rangle}{2}, \tag{1}$$

$$TK_{ADCP} = \rho_w \frac{\langle b_1'^2 \rangle + \langle b_2'^2 \rangle + \langle b_3'^2 \rangle + \langle b_4'^2 \rangle - 2(2\cos^2\theta - \sin^2\theta)\langle b_5'^2 \rangle}{4\sin^2\theta}, \tag{2}$$

for the ADV and the ADCP, respectively. Equation 2 combines the variance estimates from the ADCP transducers according to vector algebra to estimate the Cartesian 3D variance components given in Eq. 1, with the assumption of homogeneity in variance over distances comparable to the horizontal separation of the bins (Dewey & Stringer 2007). Note that TK is related to the average TKE q^2 through the relation $q^2 = TK/\rho_w$.

In a general perspective of solid-fluid interactions, energy is transferred from the shear flow to large turbulent structures, i.e., the low frequency eddies, where TKE is produced. The low frequency turbulence is considered anisotropic due to the flow geometry, but as energy cascades to the increasingly smaller structures, the directional dependence is lost, and the turbulence is considered locally isotropic and homogeneous. Energy is eventually transfered to the smallest structure of the flow where it is dissipated into heat due to viscosity. The spatial extension of the largest turbulent structures is expressed through the integral length scale L_{LL}, which is the integral of the spatial autocorrelation function $a_{LL}(z,r)$ in the vertical direction (see, e.g., Variano & Cowen (2008)). This is the correlation of the time series of a velocity component with itself at two different points in space, separated by a distance r. The autocorrelation function is computed from the along-beam velocity component of the ADCP data in the vertical direction as

$$a_{LL}(z,r) = \frac{\langle w'(z-\frac{r}{2})w'(z+\frac{r}{2})\rangle}{\sqrt{\langle w'(z-\frac{r}{2})^2\rangle\langle w'(z+\frac{r}{2})^2\rangle}}, \tag{3}$$

where r is aligned with the along-beam coordinate z for the vertical oriented beam $\mathbf{b_5}$ (Variano & Cowen 2008). Hence, the applied autocorrelation function is longitudinal as r is parallel to w. The integral length scale at a certain $z-$position is then found as

$$L_{LL}(z) = \int_0^{\delta} a_{LL}(z,r)dr, \tag{4}$$

where δ is the lag distance where $a_{LL}(z,r)$ first crosses zero (Greene et al. 2015).

Another important turbulence parameter in addition to the TKE density, frequency spectra and integral length scale is the TKE dissipation rate ϵ. In this paper, the TKE dissipation rate is estimated with three different methods, namely order-of-magnitude assessment, structure function fit and spectral fit. The latter approach is emphasized herein, but a comparison of the estimated values from all the methods is presented in Sec. 4. As a first approximation, we used the order-of-magnitude estimate

$$\epsilon = C_L(2/3q^2)^{2/3}/L_{LL}, \tag{5}$$

where $C_L = 0.5$ is a constant (Variano & Cowen 2008) and the values q^2 and L_{LL} were computed from the ADCP data.

Thereafter, the TKE dissipation rate was estimated from structure function fits. The second order longitudinal structure function D_{LL} of the velocity fluctuations in the vertical direction is calculated as

$$D_{LL}(z,r) = \langle(w'(z-r/2) - w'(z+r/2))^2\rangle, \tag{6}$$

where r is aligned with the along-beam coordinate z for the vertical oriented beam $\mathbf{b_5}$. From the restrictions imposed by the use of the ADCP, r increases incrementally with two times the ADCP bin size. In the inertial subrange, the second order structure function is related to the TKE dissipation rate ϵ by

$$D_{LL}(z,r) = C_D(\epsilon r)^{2/3}, \tag{7}$$

where $C_D = 2.1$ is a constant (Variano & Cowen 2008). Following Guerra & Thomson (2017), ϵ is estimated by solving $\overline{D_{LL}(z,r)r^{-2/3}|_{r_1}^{r_2}} = C_D\epsilon^{2/3}$, where $r_1 - r_2$ is the range with a slope close to zero in the compensated structure function $D_{LL}(z,r)r^{-2/3}$, which should be flat in the inertial subrange, and the horizontal bar denotes averaging over the range of r-values between r_1 and r_2 (indicated by the vertical bar). Minimum six points in the structure function were used to compute estimates of ϵ.

Finally, the method for estimating the TKE dissipation rate from spectral fits is explained. The velocity measurement in frequency is related to the turbulent wavenumber k through the velocity $\langle w_{adv}\rangle = 2\pi f/k$, that is the time averaged vertical speed at which the turbulence advect past the measurement instrument. Due to the cyclic flow in the present experiment, $\langle w_{adv}\rangle$ was nearly zero and is therefore substituted with w_{rms}, which is the root mean square value of the fluctuating vertical velocity component (Tennekes 1975, Zippel et al. 2018). In the inertial subrange, the flow is assumed locally isotropic and the TKE frequency spectra should be proportional to $f^{-5/3}$ according to the Kolmogorov law for developed turbulence (Kolmogorov 1941). Within the inertial subrange, the TKE frequency spectra depend only on the TKE dissipation rate ϵ and f, which represents the structure size

$$PSD_w(f) = C_S\epsilon^{2/3}f^{-5/3}\left(\frac{w_{rms}}{2\pi}\right)^{2/3}, \tag{8}$$

where C_S = 0.53 is the universal Kolmogorov constant (Sreenivasan 1995). Equation 8 implies that ϵ can be estimated from the TKE spectra (Lumley & Terray 1983), provided that the inertial subrange is resolved by the instruments.

For the ADCP, a spectrum was estimated for each bin along the vertical beam. Following Guerra & Thomson (2017), ϵ was estimated in a similar manner as in Eq. 7, i.e., by solving $\overline{PSD_w(f)f^{5/3}|_{f_1}^{f_2}} = C_S\epsilon^{2/3}(w_{rms}/2\pi)^{2/3}$, where f_1 = 0.2 to f_2 = 1.0 Hz is the range of frequencies with a slope close to zero in the compensated spectrum $PSD_w(f)f^{5/3}$, which should be flat in the inertial subrange. The uncertainty in the estimated TKE dissipation rate σ_ϵ is expressed by propagating the uncertainty in the compensated spectrum

$$\sigma_\epsilon = \frac{3\pi}{w_{rms}C_K^{3/2}}\sigma_{comp}\sqrt{\overline{PSD_w(f)f^{5/3}|_{f_1}^{f_2}}}, \tag{9}$$

where σ_{comp} is the standard deviation of the compensated spectrum over the range of frequencies $f_1 - f_2$ (Guerra & Thomson 2017).

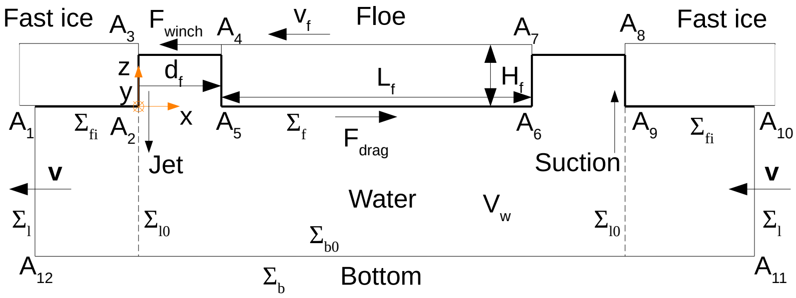

Figure 5: Scheme of the fast ice and floe and the liquid domain below.

3 Theoretical background

In this section, the moving ice floe and the surrounding water are described theoretically, and the different forces acting on the floe and the mechanisms of energy input and dissipation are identified. An idealized sketch of the towing situation is presented in Fig. 5, where an ice floe is free to move inside a pool in the fast ice. The towing force applied by the winch F_{winch} initiate floe motion and act in the same direction as the axial floe velocity $v_{f,x}$ (at the gravity center of the floe), whereas the frictional forces applied on the ice floe by the surrounding water F_{drag} act in the opposite direction. Similarly, power P is transferred to the floe from the winch (P_{winch}) and to the water from the floe (P_{drag}) due to the external forces F, where $P = |Fv_{f,x}|$. The energy balance of the floe can be described by

$$\frac{dK_f}{dt} = P_{winch} - P_{drag} - P_{coll} - P_{other}, \tag{10}$$

where $K_f = \sum_{i=1}^{3}(mv_{f,i}^2 + I_i\omega_{f,i}^2)/2$ is the kinetic energy of the floe, m and I are the mass and moment of inertia of the floe, respectively, ω_f is the angular velocity of the floe rotation around the gravity center, t is time, P_{coll} is the power dissipated in the floe collisions with the fast ice, i.e., the power of the structural energy loss and P_{other} is the power dissipated in other processes, such as losses in the towline and ice screws and waves radiating away from the floe. Equation 10 is equal to zero when it is time averaged over the period of the oscillating motion.

Now, the water volume V_w around and below the fast ice and floe bounded by the broken line $A_1 - A_{12}$ in Fig. 5 is considered. The volume boundary Σ consists of the boundary with the fast ice Σ_{fi}, the boundaries of the pool with the floe passing the points $A_2 - A_9$, the lateral boundaries of the water volume Σ_l and the bottom boundary associated with the seabed Σ_b. The submerged surface of the floe Σ_f consists of the broken line $A_4 - A_7$. The sea depth is constant, and the fast ice is extended horizontally to the infinity from the pool. It is assumed that a large-scale pressure gradient associated with the semi-diurnal tide influences the sea current below the ice with a mean horizontal velocity $\mathbf{v} = \mathbf{v}(z)$, which generates the background turbulence. According to Landau & Lifshitz (1987a) (Eq. 16.1), the kinetic energy balance of the water inside the volume V_w is written as follows

$$\frac{dK_w}{dt} = \int_{\Sigma} [\boldsymbol{\sigma}_n - K\mathbf{n}] \cdot \mathbf{v} dS - D_v, \tag{11}$$

where K_w is the kinetic energy of the water, $\boldsymbol{\sigma}_n$ is the stress vector, $\mathbf{n}$ is the outward unit normal vector at the boundary Σ, K is the density of kinetic energy, $\mathbf{v} = (u, v, w)$ is the water velocity and D_v is the rate of viscous energy dissipation. The kinetic energy of the water is determined as $K_w = \int_{V_w} KdV$, where $K = \rho_w(u^2 + v^2 + w^2)/2$ and ρ_w is the water density. The rate of viscous energy dissipation is determined by the formula $D_v = \mu \int_{V_w} (\partial v_i/\partial x_j + \partial v_j/\partial x_i)^2 dV/2$, where μ is the dynamic viscosity of water.

First, the case of a mean, steady flow due to the tidal current below a continuous fast ice is considered, where $dK_w/dt = 0$ and $K = const$. Semi-diurnal tidal current is not steady since the period is of about 12.42 h, but it is reasonable to consider it as steady over times that are much smaller than the period, which is the case here. The subscript *s* will be used to denote properties due to the steady current. In this situation, i.e., where the ice floe is not moving, Eq. 11 leads to

$$\int_{\Sigma_l} p_s \mathbf{n} \cdot \mathbf{v}_s dS + D_{v,s} = 0, \tag{12}$$

where p is the water pressure. Equation 12 states that the work of water pressure equals the energy dissipation inside the water volume V_w. The integral in Eq. 12 is negative because the water moves in the opposite direction to the pressure gradient. The remaining terms from Eq. 11 are zero. It is assumed that $\boldsymbol{\sigma}_n = 0$ at the open surface of water between the floe and the fast ice. The integral of $K\mathbf{n} \cdot \mathbf{v}$ equals zero if the surface Σ_l is extended far away from the pool where the influence of the floe on the sea current is small: the integral of $K\mathbf{n} \cdot \mathbf{v}$ equals zero due to symmetry over Σ_l and because $\mathbf{n} \cdot \mathbf{v} = 0$ at the ice, water and bottom surface over Σ_{fi} and Σ_b.

Next, the periodic back and forth motion of the ice floe is introduced. The subscript *o* will be used to denote properties due to the oscillating floe motion and the steady current. In this section, angled brackets $\langle \cdots \rangle$ are used to describe time averaging over the period of the oscillating motion T_s. Equation 11 is averaged over T_s, which leads to

$$\int_{\Sigma_l} \langle p_o \mathbf{n} \cdot \mathbf{v}_o \rangle dS - \left\langle \int_{\Sigma_f} \boldsymbol{\sigma}_{n,o} \cdot \mathbf{v}_o dS \right\rangle + \langle D_{v,o} \rangle = 0, \tag{13}$$

where the second integral is equal to the power of the floe work to move the surrounding water $\langle P_{drag} \rangle = \left\langle \int_{\Sigma_f} \boldsymbol{\sigma}_{n,o} \cdot \mathbf{v}_o dS \right\rangle$, and $\langle D_{v,o} \rangle$ is the average rate of energy dissipation.

It is assumed that $\langle p_o \mathbf{n} \cdot \mathbf{v}_o \rangle \approx p_s \mathbf{n} \cdot \mathbf{v}_s$ over the lateral surface Σ_l in Eqs. 12-13 if Σ_l is extended far away from the pool where the influence of the floe motion is small. Similarly, it is assumed that $\mathbf{v}_s \to \mathbf{v}_o$ with increasing distance from the floe. Subtraction of Eq. 12 from Eq. 13 leads to the equation

$$\langle P_{drag} \rangle = \left\langle \int_{\Sigma_f} \boldsymbol{\sigma}_{n,o} \cdot \mathbf{v}_o dS \right\rangle = \langle D_{v,o} \rangle - D_{v,s}. \tag{14}$$

The dissipation rates $\langle D_{v,o}\rangle$ and $D_{v,s}$ can be written as integrals $\langle D_{v,o}\rangle = \int_{\Sigma_b}\langle d_{v,o}\rangle dxdy$ and $D_{v,s} = \int_{\Sigma_b} d_{v,s}dxdy$, where $\langle d_{v,o}\rangle$ and $d_{v,s}$ are the area densities of the energy dissipation rates, and x and y are the horizontal coordinates. It is assumed that $\langle d_{v,o}\rangle = d_{v,s}$, far away from the floe. The difference $\langle D_{v,o}\rangle - D_{v,s}$ can be written as a sum

$$\langle D_{v,o}\rangle - D_{v,s} = \int_{\Sigma_{b0}}(\langle d_{v,o}\rangle - d_{v,s})dxdy + \int_{\Sigma_{l0}}(\langle K_o\mathbf{n}\cdot\mathbf{v}_o\rangle - K_s\mathbf{n}\cdot\mathbf{v}_s)dS, \tag{15}$$

where Σ_{b0} is the part of the sea bottom surface below the pool and Σ_{l0} is the vertical cylindrical surface separating the pool from the fast ice. The first integral on the R.H.S of Eq. 15 describes the energy dissipation rate in the water above the surface Σ_{b0}, and the second integral equals the kinetic energy transported through the surface Σ_{l0} by the sea current in unit time and dissipated outside the surface Σ_{l0}.

4 Results

The results are organized according to Eq. 10, i.e., as an energy balance of the system of interest, consisting of the ice floe and the surrounding water bounded by the fast ice. The power input to the system from the electrical winches P_{winch} is compared with the rate of energy dissipation in the floe-wall collisions P_{coll} and the total TKE rate in the surrounding water due to the floe motion, which is equivalent to P_{drag}. The two former terms are calculated as an average amount of energy, either as input or consumed per half cycle, and divided by the average duration of a half cycle to obtain the unit of power, whereas the latter term is estimated from time series of the entire experiments and is expressed as rate of energy dissipation. The reader is reminded that six experiments are included in this paper, and that each experiment contained around 10 periods of ice floe towing oscillations T_s, referred to as cycles.

4.1 Input energy

Range meter and load cell data were combined to investigate the input energy rate to the system of interest. The instantaneous power input P_{winch} was determined as the product of the floe velocity in the axial direction $v_{f,x}$ and the towing load applied by the winch F_{winch}. Figure 6 shows a part of the time series including Cycles 5-11 in Exp. 3 as an example. The cycles are marked with numbers and separated with vertical dashed lines. Negative velocity means displacement towards the south end of the pool. The load cell only provided information when the towing occurred in the $-x$-direction. The work performed by the winch on the ice floe E_{winch} during a half cycle was determined as the integral of the towing power with respect to time over the time span of the half cycle. This corresponds to the shaded areas in Fig. 6.

In each cycle, there was typically one large peak in towing power from accelerating the ice floe, succeeded by a smaller peak. The second peak was probably a consequence of additional power input needed to overcome the increasing water pressure in the closing gap. The shaded areas in Fig. 6 extend in time until collision occurs. When Cycles 1 and 5-11 are considered (Cycles 2-4 contained severe load cell dropouts), the average work applied to tow the ice floe in one

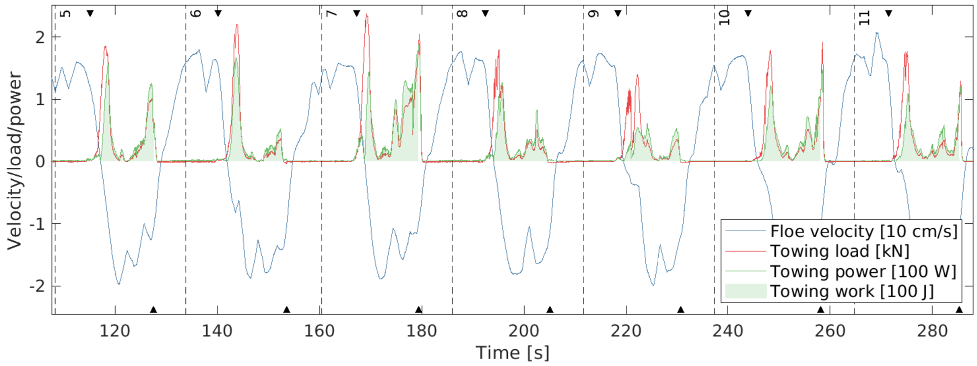

Figure 6: Part of the time series of ice floe translational velocity in the axial direction (blue), towing load (red) and towing power (green) applied by the south end winch, including Cycles 5-11 (marked with numbers and separated with vertical dashed lines) in Exp. 3. Shaded regions indicate towing work. Upward and downward-pointing triangles indicate the time of the collisions on the south and north ends, respectively.

direction E_{winch} was 428 J. One half cycle lasted on average 13.3 s, which means that the average power transfer from the winch to the ice floe was approximately 32.2 W. Due to symmetry arguments, it is assumed that the north end winch applied equal power to the system as the south end winch. The load cell was only applied in Exp. 3. It is assumed that the winch input power to the system was similar in Exps. 1-6 due to the consistency in the towing procedure.

4.2 Energy dissipation in collisions

Collisions between the ice floe and the fast ice are characterized from the uniaxial accelerometers placed on the floe. The time series of the acceleration in the x-direction from Exp. 3, presented in Fig. 3, reveal periodic recurring spikes, which correspond to impact events. Two events occurred per cycle, when the floe collided in the south and north ends of the pool. Figure 7 presents time series of the acceleration and velocity during the collision events in the eighth cycle of Exp. 3. The velocity was found by numerically integrating the acceleration with respect to time with the cumulative trapezoidal method. After the integration, a second order Butterworth bandpass filter with cutoff frequencies of 0.05 and 100 Hz was applied to remove any low frequency noise associated with the integration (Sutherland & Rabault 2016).

The collision events presented in Fig. 7 are characterized by an initial peak in the acceleration time series, which corresponds to ice floe deceleration as it approached the ice edge, followed by a smaller acceleration with opposite sign. The latter acceleration is likely due to rotation of the floe (Marchenko et al. 2021a), which could have happened if the contact faces were not perfectly parallel at the instance of impact t_{impact}. Following Li & Lubbad (2018), the time instance of impact t_{impact} occurs at the peak deceleration, and the collision start and end time, t_{pre} and t_{post}, are determined as $t_{impact} \pm \Delta t$, where Δt is set to 0.06 s from empirical observations. Hence, the duration of the peak deceleration was 0.12 s (t_{pre} and t_{post} are indicated with vertical dashed lines in Fig. 7) and the entire collision event including the initial peak deceleration and the successive acceleration lasted around 1 s. Marchenko et al. (2019b) found from ice block drop experiments that the typical peak deceleration period was 0.1 and 0.01 s for wet and dry collisions,

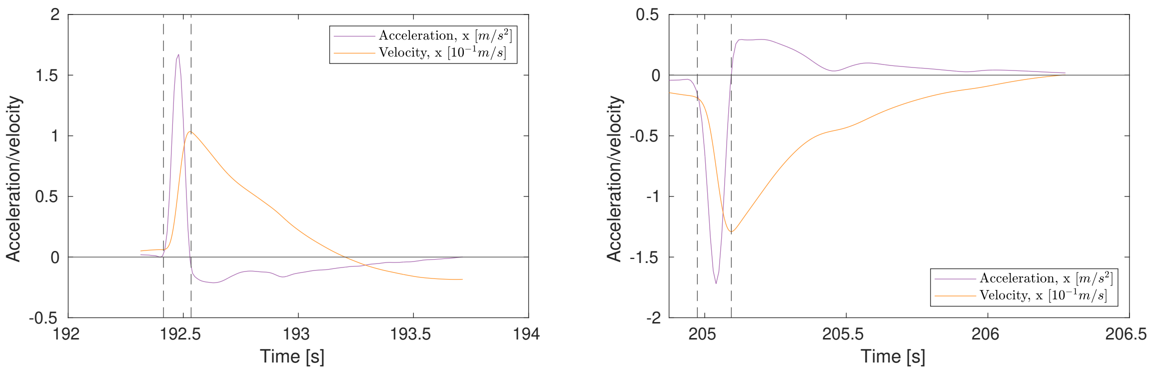

(a) The south end of the pool.

(b) The north end of the pool.

Figure 7: Collision events during the eighth cycle in Exp. 3. Ice floe acceleration and velocity (integrated acceleration w.r.t. time) in the x-direction from the uniaxial accelerometer data. Vertical dashed lines define the start and end of the collisions in the (a) south and (b) north end of the pool.

respectively. The peak deceleration amplitude in the current results is 1-2 ms^{-2} and the acceleration time series agree in general with the ice floe towing experiments of Marchenko et al. (2021a).

Close inspection of video material confirms that the collisional interaction of the ice floe and land fast ice occurred in a point of local contact, and then floe rotation influenced contacts in other places along the short end of the floe, as suggested in the previous paragraph. Figure 7 shows that the total duration of this interaction was about 1 s and that the first contact interaction corresponds to the acceleration peak extended over 0.1 s. The characteristics of this interaction is estimated using the analytical solution of the Hertz problem, which describes elastic collision of an elastic sphere of radius R and a half-space (Hertz 1882, Landau & Lifshitz 1987*b*), assuming that the elastic modulus E and the Poisson's ratio ν of the floe and the land fast ice are the same. The surface temperature of the ice was equal to the freezing point ($-1.9°$C) and the elastic modulus of sea ice with temperature close to the freezing point is $E \approx 2$ GPa (Marchenko et al. 2020). It is assumed that the Poisson's ratio is $\nu = 0.3$ (Timco & Weeks 2010). The maximum contact pressure p_{max} and the time of interaction τ are given by

$$p_{max} = \frac{1}{\pi}\sqrt[3]{\frac{6F_{max}E^{*2}}{R^2}}, \tau = 2.94\sqrt[5]{\frac{225m^2}{256E^{*2}v_cR}}, \tag{16}$$

where m is the ice floe mass, v_c is the collision velocity, $F_{max} = 1.28(E^*\sqrt{R})^{2/5}v_c^{6/5}$ and $E^* = 0.5E/(1-\nu^2)$.

Numerical estimates show that p_{max} decreases from 16 to 5 MPa, and τ decreases from 0.1 to 0.06 s when the radius R increases from 0.1 to 1.0 m. The stress level is below compression strength of ice in borehole jack tests (Timco & Weeks 2010). The time estimate shows that collisional interactions can be considered as elastic interactions. The collisional interaction between floes generates longitudinal elastic waves that are propagating over large distances in the Arctic ice (Dugan et al. 1992, Marsan et al. 2019).

Accelerometer data from the IMU were investigated for comparison and processed in the same manner as the uniaxial accelerometer data to find velocity time series. The IMU data agree in general with the uniaxial accelerometer data, although the impacts were poorer resolved due to the much lower sampling frequency. Consequently, the peak deceleration events appeared smaller and lasted longer than the ones obtained from the uniaxial accelerometers. From evaluation of the peak decelerations, Δt was set to 0.2 s for the IMU data.

A sudden change in velocity can be observed during the time of the peak deceleration Δt in Fig. 7. Following Li & Lubbad (2018), the energy dissipated in the elastic collision between floes E_{coll} can be estimated as the difference in kinetic energy $E_{coll} \approx \Delta K_f$ of the floe at t_{pre} and t_{post}. As mentioned in Sec. 2.1, the vertical modes of floe motion were negligible. Therefore, Eq. 1 of Li & Lubbad (2018), which describes the total kinetic energy of the floe, can be rewritten as

$$K_f \approx \frac{1}{2}mv_{f,x}^2 + \frac{1}{2}mv_{f,y}^2 + \frac{1}{2}I_z\omega_{f,z}^2, \tag{17}$$

where v_x and v_y are the floe translational velocities in the horizontal plane (related to surge and sway), I_z is the moment of inertia about the vertical axis that goes through the floe center of gravity and ω_z is the rotational velocity about the vertical axis (related to yaw). The ice floe mass was estimated as $m = \rho_f L_f W_f H_f$, where $\rho_f = 9 \times 10^2$ $\mathrm{kgm^{-3}}$ was the average measured sea ice density (Marchenko et al. 2021b). The moment of inertia was estimated as $I_z = m(L_f^2 + W_f^2)/12$, i.e., the tabulated value of a rectangular prism, see e.g., Spiegel & Liu (1999). The first two terms on the R.H.S. of Eq. 17 were calculated from both uniaxial accelerometer and IMU data, and the two instruments agreed. The last term was only obtained from the IMU data.

In terms of lost kinetic energy in the collisions, the contribution from surge motion was found to dominate the contributions from sway and yaw by one and two orders of magnitude, respectively. The latter two terms on the R.H.S. of Eq. 17 are therefore neglected in the following. From the uniaxial accelerometer data, the dissipated energy in one collision event E_{coll} was found to be 32.1 J on average over the 11 cycles in Exp. 3. Considering the average duration of a half cycle, the mean power dissipated due to collisions P_{coll} was 2.4 W, which corresponds to 7.5% of the total input energy rate P_{winch}. The accelerometers were deployed together with the load cell, i.e., only in Exp. 3. As mentioned earlier, all the experiments were very consistent in terms of ice floe motion. Hence, it is assumed that the rate of energy dissipated in the collisions was similar in Exps. 1-6.

4.3 Optical measurements of jet generation

Although the acoustic velocimeters were only deployed on the fast ice next to the pool and in the ice floe center, the ROV and rising bubbles setup provide information on the flow structures below the floe and the fast ice. Figure 8 presents four images taken with the ROV camera, which show the ice floe colliding with the south end of the pool during the 11th cycle in Exp. 3 (the video from which the images are extracted is available here: https://vimeo.com/700522062). The camera axis is approximately aligned with the y-axis. The ice floe approaches the fast ice in a)-b), collision occurs

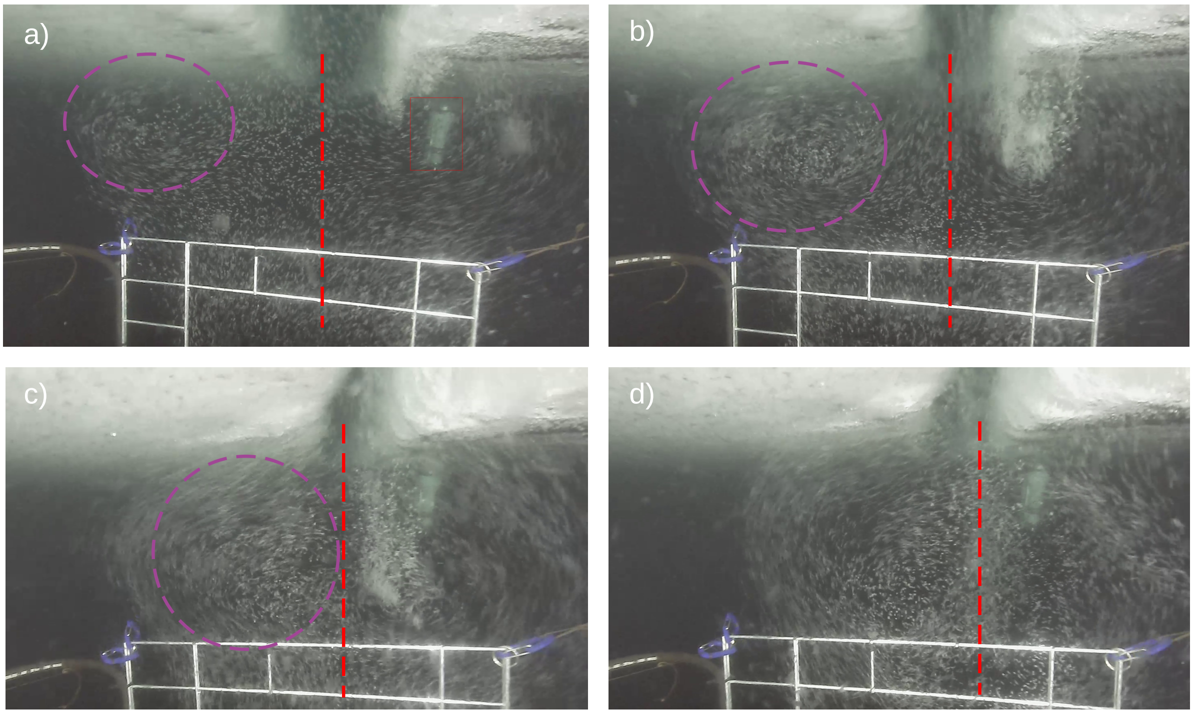

Figure 8: Evolution of a downward water jet as the ice floe (left) approaches the fast ice (right) during the 11th cycle in Exp. 3. The dashed red lines indicate the flow axis and the dashed magenta ellipsis indicate the left hand side vortex (rotation in the clockwise direction). The time span between each frame a)-d) is 0.5 s. The red rectangle in panel a) indicates the ADV, which was positioned behind the bubble curtain. The ADCP (positioned in front of the ADV) is not visible on the images.

around c) and the floe moves away from the fast ice in d). A downward jet is forming in the closing gap with a large eddy structure on each side in the axial direction. The eddy structure remains while water starts to flow upwards into the opening gap after the collision. The length of the metal grid in the lower part of the image is 0.55 m, meaning that the total jet diameter, including the resulting turbulent cloud, is in the order of 1 m. As the jet evolves, the vortex centers move towards the (vertical) flow axis. The horizontal distance from the flow axis to the vortex center is approximately 0.1-0.3 m.

Over the last couple of decades, particle image velocimetry (PIV) has been adapted to field experiments to investigate flow kinematics in the ocean, see e.g Smith et al. (2002), Bertuccioli et al. (1999), Løken et al. (2021a). PIV was performed on consecutive ROV image pairs with the in-house HydrolabPIV software developed at the University of Oslo (Kolaas 2016). The processing was performed with 48×48 pixel subwindows with 50% overlap. A linear pixel-to-world coordinate transformation was achieved with the mesh-points of the metal grid. The mean vertical buoyancy driven bubble velocity was found in a reference run with calm water and subtracted from the velocity field obtained in the jet. Further details on the experimental setup and processing scheme can be found in Løken et al. (2021a). Figure 9 presents the jet 2D velocity field in the xz-plane in Exp. 3, 0.33 s after Fig. 8c, which means that the ice floe was moving away from the fast ice and a suction motion into the opening gap was already initiated. As in Fig. 8, two large eddies can be seen with centers approximately 10 cm from the flow axis and water flows upward into

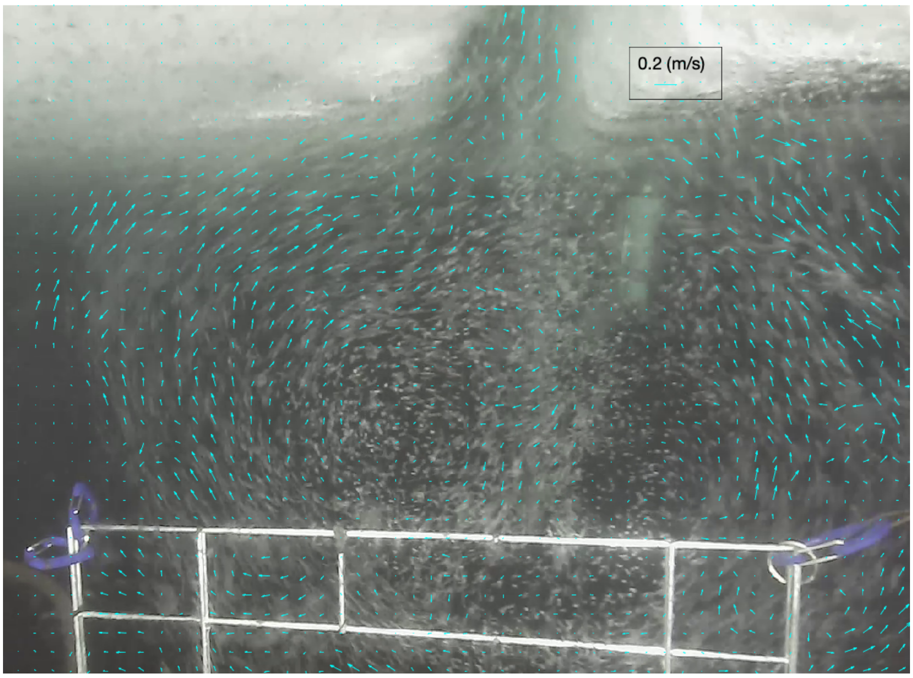

Figure 9: Downward jet processed with PIV to obtain velocity vectors. The image frame was taken 0.33 s after Fig. 8c. The magnitude of the velocity vectors is indicated in the legend.

the opening gap. Circular water motion is evident up to 0.5 m from the flow axis. Smaller turbulent structures were also resolved and can be observed within the jet domain. This observation, particularly the short distance from the flow axis to the vortex center, indicates that the ADCP probably captured the most dominating flow structures when it was placed 0.25 m from the pool edge but may have failed to do so when placed further away.

4.4 Turbulent kinetic energy dissipation

From the fluctuating vertical velocity component of the ADV and all the ADCP bins, TKE spectra were estimated with the Welch method described in Sec. 2.2. All the cycles that were measured by both instruments were included in the calculations. The bins corresponding to the 15 cm closest to the instrument head showed some unphysical behavior, probably due to transducer ringing (Nystrom et al. 2007), and were therefore discarded. Figures 10a-f present the spectra from Exps. 1-6, respectively, where only 10 ADCP bins evenly distributed over the 2 m deep profile are presented to increase the readability. The thicker orange spectra in Figs. 10a-e are produced from the ADV, which was not deployed in Exp. 6 when the ADCP was placed in the ice floe center. Most of the spectra exhibit peak frequencies around 0.04 Hz, which correspond to the ice floe surge period of approximately 26 s. The gray shaded regions illustrate the range of frequencies $f_1 - f_2$ over which the compensated spectra were averaged in order to estimate the TKE dissipation rate, i.e., where a slope proportional to $f^{-5/3}$ is expected in accordance with Eq. 8.

The spectra are proportional to $f^{-5/3}$ over a wide range of frequencies, meaning that both instruments were able to resolve the inertial subrange. Typically, ADCP data quality deteriorates as the distance from the instrument increases,

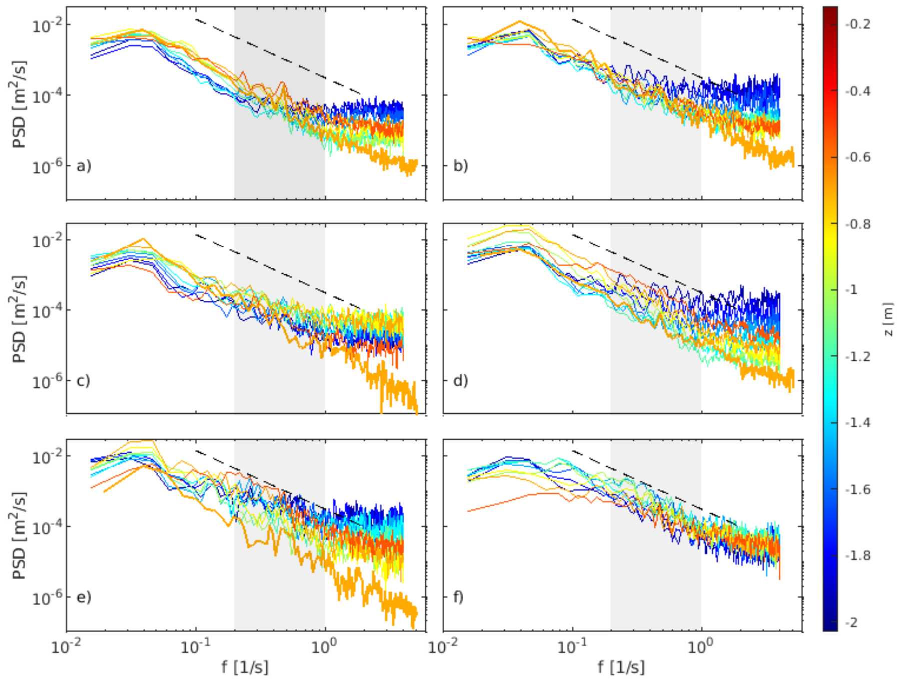

Figure 10: Turbulent kinetic energy spectra obtained with the ADCP from various depths in Exps. 1-6 shown in a)-f), respectively. The black dashed lines show the theoretical $f^{-5/3}$ slope. The ADV spectra are shown as thick orange lines in a)-e), but the ADV was not deployed in Exp. 6 when the ADCP was placed in the ice floe center. The shaded regions show the range of frequencies over which the compensated spectra were averaged to estimate ϵ.

either as decreasing beam correlation or increasing instrument noise. If the signal is obscured by Doppler noise, the spectra appear flat towards the higher frequencies. In Fig. 10, the ADCP noise floor is in general $\sim 10^{-5}$ m^{2}s^{-1} close to the transducer and $\sim 10^{-4}$ m^{2}s^{-1} towards the end of the profile, with some exceptions, e.g., in Exp. 3 when the correlation was low (see Fig. 12a). The ADV spectra exhibit a noise floor at $\sim 10^{-6}$ m^{2}s^{-1}. In Exps. 1-5, the spectra from the bins below $z \approx -1.2$ m flatten out within the gray shaded region, which illustrates that the instrument noise level exceeded the TKE level for $f < f_2$. These data are not physical, hence not used to estimate ϵ, which is only estimated for $z > -1.2$ m in Exps. 1-5 from Eq. 8. However, all the spectra in Exp. 6 are approximately proportional to the $f^{-5/3}$ slope within the shaded region. Therefore, ϵ was estimated along the entire profile in Exp. 6.

The autocorrelation function $a_{LL}(z, r)$ was computed from the full time series of the vertical fluctuating velocity component of the ADCP data at the vertical position $z = -0.58$ m with Eq. 3. Three examples are presented in Fig. 11a, where the distance r spans from 0 to 0.8 m. The integral length scale L_{LL} is obtained with Eq. 4, and corresponds to the shaded area. In Exps. 2 and 6, a_{LL} reaches a flat plateau around zero well within the range of r, while zero is just reached within the range in Exp. 4. Integral length scales from all experiments are presented in Table 3, and the values from Exp. 1-5 agree well with the large eddy structures visible in Figs. 8-9. Due to the poor ADCP data quality below $z \approx -1.2$ m, as shown in Figs. 10-12, combined with the fact that r spanned over a large portion of the

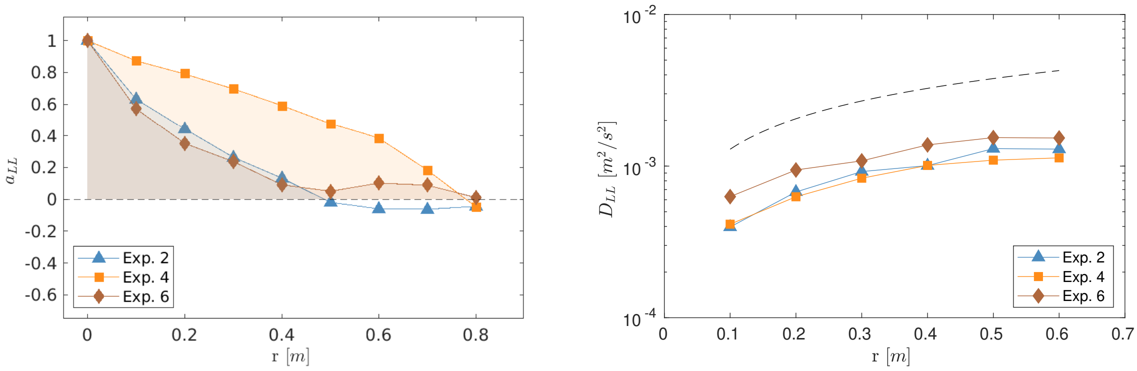

(a) Autocorrelation function.

(b) Structure function.

Figure 11: Spatial autocorrelation function and structure function calculated at the vertical position $z = -0.58$ m for one experiment at each ADCP position. The shaded area in a) corresponds to the respective integral length. The black dashed lines in b) shows the theoretical $r^{2/3}$ trend.

Exp.	Re	L_{LL} [m]	ϵ_L [m^{2}s^{-3}]	ϵ_D [m^{2}s^{-3}]	ϵ_S [m^{2}s^{-3}]
1	0.96×10^5	0.28	9.00×10^{-5}	1.10×10^{-4}	3.97×10^{-5}
2	0.95×10^5	0.21	1.20×10^{-4}	2.59×10^{-4}	9.91×10^{-5}
3	0.91×10^5	0.09	2.56×10^{-4}	3.84×10^{-4}	1.40×10^{-4}
4	1.09×10^5	0.48	7.70×10^{-5}	2.33×10^{-4}	6.22×10^{-5}
5	1.17×10^5	0.37	1.22×10^{-4}	4.29×10^{-4}	1.22×10^{-4}
6	2.01×10^5	0.19	1.20×10^{-3}	3.90×10^{-4}	4.65×10^{-4}

Table 3: Turbulence properties estimated at the vertical position $z = -0.58$ m. Column 4-6 are estimates of the TKE dissipation rate obtained from the methods: order-of-magnitude estimate, structure function fit and spectral fit, respectively. The values of ϵ_L and ϵ_S are rather similar, with some exceptions, while ϵ_D is about 3 times greater than ϵ_S, with the exception of Exp. 6, where they are similar.

good-quality data profile, the integral length scales were only estimated in one vertical position. The only exception is Exp. 6, where the data quality was good along almost the entire measurement span, and the integral length scales were found to be $L_{LL} = [19, 16, 25, 15, 9, 7]$ cm for vertical positions spanning from $z = -0.58$ m to $z = -1.58$ m with 20 cm increments.

The TKE dissipation rates were estimated from assessing order-of-magnitudes with the scaling law from Eq. 5. These results are presented under the name ϵ_L in Table 3. Structure functions $D_{LL}(z, r)$ were computed with Eq. 6 for the same data and vertical position as the integral length scales. Examples are presented in Fig. 11b, where r spans from 0.1 to 0.6 m. All the structure functions (including the ones not shown) have slopes that are approximately proportional to the theoretical $r^{2/3}$ slope expected in the inertial subrange, and TKE dissipation rates were estimated with the structure function fitting from Eq. 7. The results are summarized in Table 3 under the name ϵ_D.

Finally, the TKE dissipation rates were estimated with the spectral fitting from Eq. 8. The results at the vertical position $z = -0.58$ m are summarized in Table 3 under the name ϵ_S. In general, the three different methods for estimating the TKE dissipation rate yield results in the same order of magnitude. The values of ϵ_L and ϵ_S are rather similar, with the

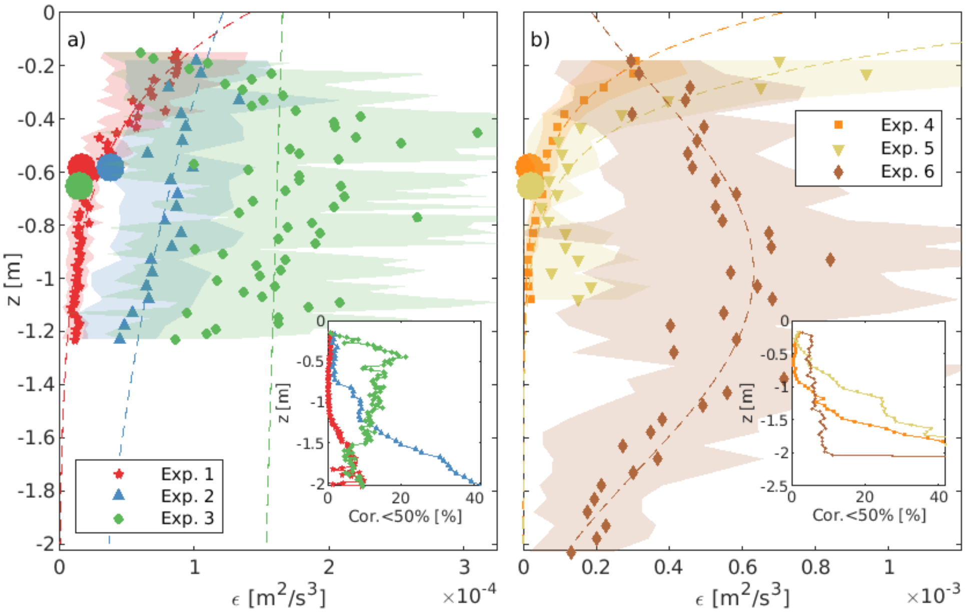

Figure 12: Estimated TKE dissipation rate profiles. a) ADCP placed 0.50 m from the pool edge in Exp. 1 (red), 2 (blue) and 3 (green). b) ADCP placed 0.25 m from the pool edge in Exp. 4 (orange) and 5 (yellow) and on the ice floe center in Exp. 6 (brown). In Exps. 1-5, ϵ was not estimated for $z < -1.2$ m due to the high instrument noise level. Dashed lines show curve fits to the ADCP data ϵ_{fit}. Confidence intervals σ_ϵ are indicated with shaded regions. The inset plots show the vertical beam correlation data for the ADCP profiles (percentage of time series with correlation < 50%). ADV data are presented as large dots.

exceptions of Exps. 1 and 6, where ϵ_L is about 2-3 times greater than ϵ_S, while ϵ_D is about 2-3 times greater than ϵ_S, with the exception of Exp. 6, where the values are similar. The method of spectral fits offer the advantage of estimating values along the entire measurement profile of the ADCP, and allows for comparison with ADV point data. Therefore, results from the spectral fitting is used in the rest of the paper, and the TKE dissipation rate is simply referred to as ϵ, although ϵ_S is implied.

Figures 12a-b present the estimated TKE dissipation rates ϵ from Exps. 1-3 and 4-6, respectively. The inset plots show the percentage of the ADCP time series where the vertical beam correlation was below the manufacturer recommendation (50%). In Exp. 3, the beam correlation was below the recommended value more than 10% of the time, see Table 4, which is an indication of poor data quality. This is probably why a large data scattering can be observed along the ϵ profile in Exp. 3. The profiles appeared to decay exponentially with depth when the ADCP was placed on the fast ice close to the pool wall, i.e., in Exps. 1-5, perhaps apart from Exp. 3 where the data quality was poor. Therefore, exponential functions on the shape $\epsilon_{fit} = ae^{-bz}$, where a and b are estimated parameters, were fitted to the data with nonlinear regression by means of iterative least squares and plotted as dashed lines in Fig. 12. A fourth order polynomial function was fitted to the estimated ϵ values in Exp. 6. The standard deviations of $\epsilon - \epsilon_{fit}$ along the profile are presented in Table 4 as a measure on the accuracy of the curve fits. Especially the relative standard deviation, which is normalized over the mean ϵ, shows that ϵ clearly decay exponentially with depth in Exps. 1, 2 and 4.

Exp.	Corr. < 50% [%]	Mean ϵ [$\mathrm{m^2s^{-3}}$]	Std. ϵ [$\mathrm{m^2s^{-3}}$]	Rel. std. ϵ [%]	$\pm\sigma_\epsilon$ [%]	d [$\mathrm{Wm^{-2}}$]
1	0.5	3.4×10^{-5}	6.1×10^{-6}	17.8	49.6	5.7×10^{-2}
2	4.3	8.3×10^{-5}	1.2×10^{-5}	15.0	49.4	1.5×10^{-1}
3	12.7	1.6×10^{-4}	4.7×10^{-5}	28.9	63.5	3.3×10^{-1}
4	2.3	8.4×10^{-5}	1.5×10^{-5}	18.4	45.6	1.7×10^{-1}
5	8.1	2.4×10^{-4}	1.3×10^{-4}	53.1	71.1	4.4×10^{-1}
6	5.3	5.2×10^{-4}	8.6×10^{-5}	16.6	66.4	9.2×10^{-1}

Table 4: Statistics on ADCP beam correlation and estimated area density of TKE dissipation rate. Columns 2-6 apply for $z > -1.2$ m and column 7 applies for the entire profile, i.e., $z > -2.0$ m. Column 2 is the percentage of the time series where the beam correlation was less than 50%, averaged over all bins. Column 3 is the mean ϵ averaged over all bins. Column 4 is the standard deviation of $\epsilon - \epsilon_{fit}$. Column 5 is the relative standard deviation, i.e., Column 4/Column 3. Column 6 is the average uncertainty in the estimated ϵ, given in Eq. 9 and the shaded area in Fig. 12. Column 7 is the area density of TKE dissipation rate from the ϵ_{fit} profiles.

It is desirable to quantify the total energy dissipated in turbulence in the water affected by the ice floe motion. The ϵ_{fit} values were therefore numerically integrated with the trapezoidal method over the entire profile to find the area density of TKE dissipation rate $d = \rho_w \int_{-2}^{0} \epsilon_{fit}\, dz$ [$\mathrm{Wm^{-2}}$]. Confidence intervals for the estimated ϵ, i.e., σ_ϵ estimated from Eq. 9, are illustrated as shaded regions in Fig. 12. Estimated d and the average percentage of the uncertainties with respect to the fitted curves are listed in Table 4. Estimated ϵ from the ADV spectra are presented as large dots in Fig. 12. Some of the dots are displaced a bit in the vertical direction to increase the readability, even though the measurement volume was located at $z = -0.58$ m in all the experiments. The estimated values from the ADV were in general smaller than the values from the ADCP. The reason for this is unknown in Exps. 1-3 but is probably that the ADCP was placed closer to the pool, where the TKE level is expected to be higher, in Exps. 4-5. Ideally, the ADV should have been mounted at the same x-position as the ADCP, but this was not possible with the ADV tripod.

The density of TKE profiles TK from the ADCP and single values from the ADV obtained from Eqs. 1-2 are presented in Fig. 13, where solid markers indicate measured data and solid lines indicate data corrected for instrument noise. There is good agreement between the ADCP and the ADV, especially in Exps. 1-3 where the instruments were placed at the same x-location. As previously discussed, it is expected that the TKE level was higher closer to the pool edge, which probably explains the lower values obtained from the ADV in Exps. 4-5. The density of TKE profiles approach zero with increasing depth and are therefore numerically integrated over the profile to find the area density of TKE $TK_z = \int_{z_2}^{z_1} TK\, dz$ [$\mathrm{Jm^{-2}}$], where z_1 is the first ADCP bin and z_2 is the last considered bin. The profiles show some negative values and other unphysical behavior in depths below z_2, which is set to -1.2 and -2 m in Exps. 1-5 and 6, respectively, in consistency with Figs. 10-12. The TK_z values are listed in Table 5.

A single velocity that is representative for all three components u_{rep} can be expressed as $u_{rep} = \sqrt{2q^2/3}$ (Variano & Cowen 2008). The representative velocity was calculated from the TK values from the ADCP presented in Fig. 13, with the relation $q^2 = TK/\rho_w$. From this representative velocity and a representative length scale for the experiment L_{l0}, the Reynolds number was computed as $Re = u_{rep}L_{l0}/\nu_w$, where $L_{l0} = 6$ m is the approximate length of the pool

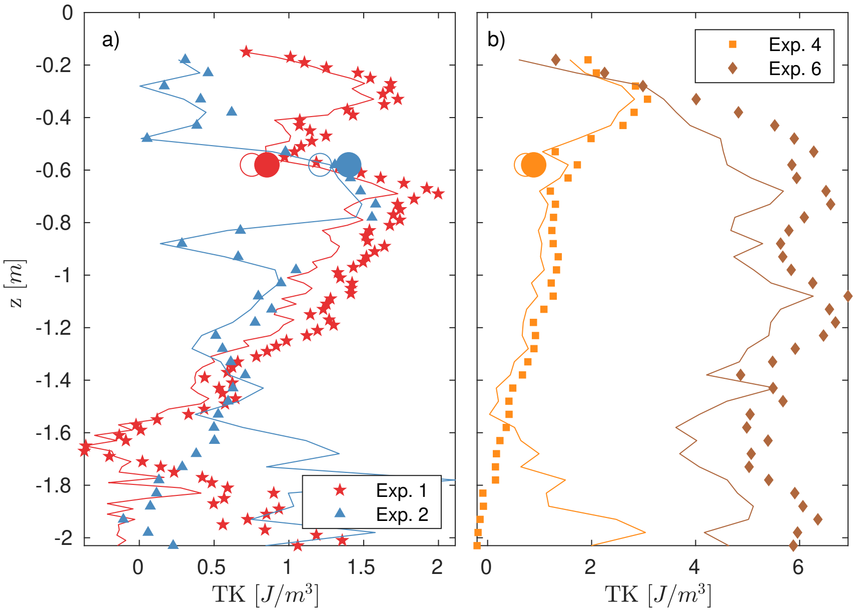

Figure 13: Estimated density of TKE profiles. a) ADCP placed 0.50 m from the pool edge in Exps. 1 (red) and 2 (blue). b) ADCP placed 0.25 m from the pool edge in Exp. 4 (orange) and on the ice floe center in Exp. 6 (brown). Experiments 3 and 5 showed the same behavior as Exps. 1-2 and 4, respectively, but these are not included to increase readability. ADV data are presented as large dots. Solid markers show measured values and lines show values corrected for instrument noise.

and $\nu_w = 1.84 \times 10^{-6}$ m^{2}s^{-1} is the kinematic viscosity of seawater. The values listed in Table 3 are consistent in Exps. 1-5, with a small increase when the ADCP was placed closer to the pool, and about two times greater under the center of the ice floe in Exp. 6.

Turbulence properties from the tidal current were investigated to find the ambient turbulence level in the boundary layer below the ice. Reference runs of ADCP time series before each experiment, i.e., when the ice floe was not moving, were considered. The mean horizontal current speed U_{mean} and direction U_{dir}, averaged over bins above $z = -1.2$ m, as well as the duration of the reference runs, are summarized in Table 5. The direction is defined as clockwise rotation about the x-axis and the mean current direction was approximately in the y and $-y$-direction in Exps. 1-5 and 6, respectively. The ADCP was usually started right before the experiments, hence the short reference run time series.

Only in Exp. 1, the reference run was long enough to estimate the ambient area density of TKE dissipation rate d_{amb} and the ambient area density of TKE $TK_{z,amb}$. However, U_{mean} was consistent in the order of 10^{-2}ms^{-1} over Exps. 1-5, so it is reasonable to assume that d_{amb} and $TK_{z,amb}$ were similar in these experiments. In Exp. 6 on the other hand, U_{mean} was smaller, in the order of 10^{-3}ms^{-1}. Nevertheless, the values of d_{amb} and $TK_{z,amb}$ obtained in Exp. 1 are used as conservative estimates for all the experiments. Both parameters are resulting from the tidal current and are listed in table 5. Depending on the experiment and the location of the ADCP, d_{amb} was 1.4-22.8% of d, and $TK_{z,amb}$ was only 0.8-8.1% of TK_z. In the following, d_{amb} and $TK_{z,amb}$ due to the mean tidal current are subtracted from

Exp.	U_{mean} [mm/s]	U_{dir} [°]	Time [s]	d_{amb} [Wm^{-2}]	TK_z [Jm^{-2}]	$TK_{z,amb}$ [Jm^{-2}]
1	7.9	253	485	1.3×10^{-2}	1.3	6.5×10^{-2}
2	4.5	253	75	-	0.8	-
3	8.0	234	175	-	1.2	-
4	5.4	267	170	-	1.5	-
5	5.4	267	170	-	0.9	-
6	1.4	104	190	-	8.4	-

Table 5: Ambient flow with mean horizontal current and direction and length of the reference run time series (columns 2-4). Experiment 4 and 5 were conducted within one hour and it is assumed that the tidal conditions were similar. Column 5 is the ambient area density of TKE dissipation rate. Area density of TKE during towing and due to the tidal current are listed in Column 6 and 7, respectively. d_{amb} and $TK_{z,amb}$ were only estimated in Exp. 1 due to sufficient duration of the reference run time series.

d and TK_z, respectively, which contain TKE from the moving floe and the tidal current, so that $d = d - d_{amb}$ and $TK_z = TK_z - TK_{z,amb}$. Henceforth, focus is directed towards the TKE dissipation rate due to the moving floe.

The total TKE dissipation rate $D = dS_{b0}$, where S_{b0} is the horizontal area of the pool, describes the rate of TKE dissipation due to the ice floe motion in the water volume below S_{b0}, and is analogous to the first integral in Eq. 15. The total TKE advection rate $TK_{adv} = TKU_{mean}S_{l0}$ describes the rate of TKE due to the floe motion that is transported away from the water volume below S_{b0} due to the mean current speed U_{mean} and dissipated elsewhere, and is analogous to the second integral in Eq. 15. S_{l0} is the area of the vertical, cylindrical surface separating the pool from the fast ice, projected on a plane with normal vector parallel to U_{dir}. As the mean horizontal current direction was roughly parallel to the y-axis, S_{l0} is approximately parallel to the xz-plane. Since TK is already integrated over z to obtain TK_z, $TK_{adv} = TK_zU_{mean}L_{l0}$, where L_{l0} is the length of S_{l0} in the x-direction, i.e., $L_{l0} \approx 6$ m.

In order to accurately quantify the total TKE dissipation due to the moving ice floe, the ADCP should have been deployed at many locations around the pool and on the ice floe, so that D and TK_{adv} could have been estimated with a high spatial resolution in the horizontal plane. An attempt is still made to estimate the total TKE dissipation rate D and the total TKE advection rate TK_{adv}. From Fig. 12, it is clear that the profiles of TKE dissipation rate are very different in the gap between the floe and the fast ice, where ϵ decay exponentially with depth, and below the floe itself, where ϵ first increase and then decay with depth after a maximum is reached at $z \approx -1$ m. The former profiles are associated with the jet and suction motion induced in the collisions, while the latter profile is associated with the turbulence below the floe. This difference is also apparent for the profiles of the density of TKE in Fig. 13. Therefore, the representative area and length are separated so that $D = d_fS_f + d_{gap}S_{gap}$ and $TK_{adv} = TK_{z,f}U_{mean}L_f + TK_{z,gap}U_{mean}L_{gap}$, where the notation f indicates the horizontal area and length of the ice floe, and *gap* indicates the horizontal gap area and length in the x-direction.

It is assumed that the ϵ and TK profiles obtained in Exp. 6 are representative for the TKE below the entire ice floe, hence $S_f = 12$ m^2, $L_f = 4$ m, $d_f = d_6$ and $TK_{adv,f} = TK_{adv,6}$. From Figs. 8-9, it can be observed that the jet diameter (and the resulting turbulent cloud) is ~ 1 m, and it is assumed that the jet extension in the y-direction is equal

Exp.	D [W]	TK_{adv} [W]	Total TKE rate [W]
1	0.26	2.0×10^{-2}	0.28 ± 0.14
2	0.82	0.7×10^{-2}	0.83 ± 0.41
3	1.90	1.8×10^{-2}	1.92 ± 1.22
4	0.94	1.6×10^{-2}	0.96 ± 0.44
5	2.56	0.9×10^{-2}	2.57 ± 1.83
6	10.88	4.7×10^{-2}	10.93 ± 7.26

Table 6: Total TKE dissipation rate due to ice floe motion. The uncertainties in the estimated ϵ (Column 6 in Table 4) are imposed on the intervals given in the total TKE rate. The total TKE rate from Exp. 6 should be combined with any of Exps. 1-5 to describe the complete experimental geometry.

to the width of the floe W_f and that a similar jet is produced in the gap on the north end of the floe, hence $S_{gap} = 6\ \mathrm{m}^2$ and $L_{gap} = 2\ \mathrm{m}$, which is in agreement with the total gap area and length in both short ends of the pool. As discussed in Sec. 4.3, the ADCP data obtained at the shortest distance from the pool, i.e., in Exps. 4-5, are probably a better realization of the flow happening in the gap than further away from the pool. Out of these two, the most correlated beam measurements, the least uncertainties in the estimated ϵ and the most cycles were obtained in Exp. 4. Therefore, it is assumed that the ϵ and TK profiles obtained in Exp. 4 are representative for the TKE in the entire gap area, hence $d_{gap} = d_4$ and $TK_{adv,gap} = TK_{adv,4}$. With these assumptions, $D = 11.8$ W, where the weighted uncertainty from σ_ϵ is $\pm 64.6\%$. Similarly, $TK_{adv} = 0.06$ W. The total TKE rate due to the floe motion $D + TK_{adv} = 11.9$ W, which corresponds to Eq. 15, is estimated to be 36.9% of the input power P_{winch}. The total TKE rate from all the experiments are summarized in Table 6. The listed uncertainties are associated with the estimated ϵ values found from Eq. 9. However, these figures are based on the assumption that the estimated values from single measurement locations are representative for the entire area of the floe and the gap, respectively. The different sources for uncertainty are further discussed in Sec. 5.

5 Discussion

The results presented in the previous section provide a step towards understanding the mechanisms of energy dissipation related to the two dynamical processes of relative water-ice motion and ice-ice collisions. Although the experimental setup is a simplification of the complex reality in the MIZ, e.g., by the fact that the orbital wave motion is absent, the period of the oscillating motion of the floe is greater than that of the typical waves found in the MIZ, and the floe is sawed in a rectangular and not an irregular shape, there are similarities to previous observations in the nature. Smith & Thomson (2020) observed pancake floes subjected to waves with periods in the order of 10 s in the Beaufort Sea MIZ, and found that the relative water-ice and floe-floe velocities were both in the order of 0.1 m/s, which is similar to the relative velocities used in the present paper. The relative velocities are the key kinematic parameters for describing the turbulence produced by the floe motion (Smith & Thomson 2020). Smith & Thomson (2019) observed turbulent velocity fluctuations with the magnitude of a few cm/s just below pancake ice in the Ross Sea MIZ. Similarly, the magnitude of the turbulent velocity fluctuations measured in the present paper, which can be seen in Fig. 4, were in the order of 1 cm/s. Collisions occurred approximately every 13 s in the present experiment. McKenna & Crocker (1992) reported that floe collisions were closely related to the wave cycle for medium sized ice floes (in the order of 10 m wide) subjected to waves with period around 10 s in the Labrador Sea MIZ. Martin & Becker (1987, 1988) investigated large ice floes (in the order of 10^2 m wide) heavily concentrated in the Greenland and Bering Sea MIZ and found that collision events in general recurred with the period of the ocean swell, which was 10-18 s. They reported that the longest observed duration of a series of consecutive collisions was in the order of minutes. Smith & Thomson (2020) used the assumption of floe collisions recurring with the wave period as an upper bound to the associated energy dissipation.

As the ice floe was towed back and forth in the pool, an oscillating flow was generated in the surrounding water due to the shear at the water-ice interface. In the TKE spectra shown in Fig. 10, these large-scale fluctuations appear around the peak frequency of 0.04 Hz, corresponding to periods around 26 s, i.e., the mean duration of a cycle T_s. Two different mechanisms generated turbulence in the pool, the drag associated with the relative water-ice velocity, and the downward jet injection and upward suction of fluid in the gap. The former creates a turbulent boundary layer below the oscillating floe, which can be observed in the TKE dissipation rate ϵ profile in Exp. 6 presented in Fig. 12, where the maximum value occurs in the water layer extended 0.6-1.4 m below the ice bottom. This is likely to occur around natural ice floes due to wave induced motion of water particles relative to the ice, and comprises turbulent friction on the underside of the ice and the wake behind the sharp edges of the floe, i.e., skin friction and form drag, respectively (Kohout et al. 2011). The effect of surface roughness of the ice floe on turbulence generation has not been considered in the present paper, but is relevant to the problem and deserves further investigations in future studies. The latter induces turbulence associated with collisions that rapidly decays with depth, as seen in the ϵ profiles in Exps. 1-5, which also may occur in a dense floe field exposed to waves (Rabault et al. 2019). Note that the epsilon profiles in Exps. 1-5 and 6 comprise turbulence from both the jet and suction motion and towing back and forth, respectively, as the entire time series including all cycles were used.

It was found that 36.9% of the mean measured power input to the system P_{winch} was transferred from the ice floe to the water and dissipated in turbulence, either directly below the system or advected away from the system with the mean horizontal current. However, a large uncertainty is associated with this estimate, and it should be used with caution. More than 80% of the total TKE rate due to the floe motion occurred under the ice floe, based on the information acquired in Exp. 6, which is associated with the relative water-ice velocity and floe drag. The data quality was good in this case, but the statistical confidence is reduced due to the fact that this experimental setup was only repeated once. In addition, the average uncertainty in the estimated TKE dissipation rate $\sigma_{\epsilon,6}$ was 66.4%. Due to the lack of further measurements, it was assumed that the area density of TKE dissipation rate d was uniform over the area of the floe, which is probably a large simplification of reality. The ϵ profiles in Exps. 1-5, associated with the downward jets and upward suction motions, are qualitatively consistent in the sense that they decay exponentially with depth, although the quantitative discrepancies, expressed through d in Table 4, are considerable. Note that the turbulence induced by the

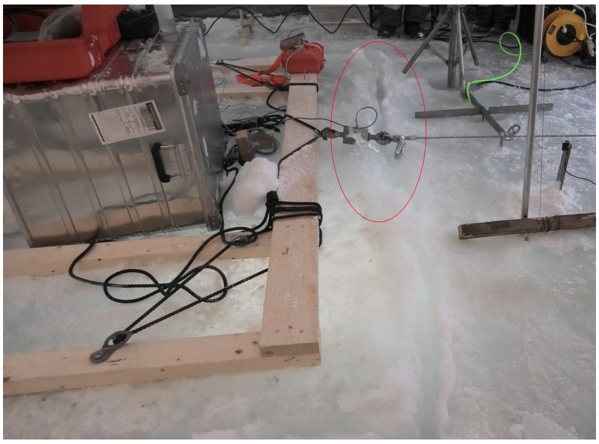

Figure 14: Owerwash immediately after a collision event. The red circle marks the erupting water jet.

shear flow in the gap between the fast ice and the lateral sides of the floe was not measured and has not been accounted for.

Approximately 7.5% of the of the mean power input P_{winch} was on average absorbed in the collisions between the ice floe and the pool walls P_{coll}, probably in mechanisms such as elastic deformation of the ice and erosion/slush production (Herman 2018, Herman et al. 2018). Figure 14 shows an image of a collision event where the walls of impact have been deformed and slush is building up on the topside of the ice. Note that the average power of the ice floe surge motion P_s, given in Appendix B, is similar to P_{coll}. Previous studies have concluded that energy dissipation due to floe collisions account for a significant part of the wave attenuation, but it is not the dominating mechanism. Shen & Squire (1998) found from modeling that energy absorption for typical ocean swell periods arising from collisions between adjacent ice floes in the order of 1 m in a dense pancake ice field is the second most dominating mechanism in terms of energy dissipation, after TKE in the water column. Li & Lubbad (2018) presented wave tank experiments with ice floes in the order of 1 m, which suggested that approximately 10% of the wave energy loss was dissipated in inelastic collisions between adjacent floes.

Induced TKE and elastic collisions were estimated to dissipate approximately 45% $\pm$23.7% of the total input energy rate, hence these mechanisms do not account for all dissipation processes. Another possible loss is the generation of outgoing surface waves in the pool due to the floe motion, which is directly associated with the damping force of the body (Squire et al. 1995). Surface waves induced by the floe surge motion have periods equal to that of the cyclic motion of the floe, i.e., $T_s \approx 26$ s, and it is expected that these long waves travel away from the pool. However, the pressure sensor integrated in the ADV showed no oscillations with periods around 26 s, so the surge-induced waves must have been small. The findings of Marchenko et al. (2021a) suggest that short surface waves are produced from collision events. If such waves were generated in the present experiments, they were probably not visible since the floe covered almost the entire pool width. Short surface waves with periods <1 s were observed visually before the collision events in the axial gaps between the floe and the fast ice, which may be associated with the eigenmodes or seiche motion in the pool. Floe oscillations with periods around 2 s were detected by the uniaxial accelerometers in the horizontal directions, as can be seen in the time series presented in the lower panel of Fig. 3, and by the IMU in the vertical direction, as shown in Fig. 15 in Appendix B. These oscillations may be associated with the piston modes of water oscillations in the lateral gaps between the floe and the fast ice and/or the natural oscillation of the floe in the vertical direction, meaning that the surge oscillations may have induced small oscillations in the vertical direction through nonlinear processes. The frequency of the piston mode wave oscillations f_p in an oscillating water column can be described by $2\pi f_p = \sqrt{g/h}$, where h is the height of the water column (Baudry et al. 2013). When H_f is substituted with h, $f_p = 0.5$ Hz is obtained. The natural frequency of the floe in the vertical direction f_h can be estimated as $f_h \approx \sqrt{\rho_w g/(\rho_f H_f(1 + m_{ad}/m))}/2\pi \approx 0.47$ Hz, where $m_{ad} \approx 2955$ kg is the added mass of the floe in the vertical direction, which is calculated with Eq. 13 in Marchenko et al. (2020). The estimated f_p and f_h both agree with the period of the accelerometer recorded floe oscillations. Note that the estimated power of the heave motion (0.1 W) was small compared to, for example, the estimated power of the surge motion (2.3 W), as shown in Appendix B. Overwash or water jets were also observed as a consequence of the collisions, which is another damping mechanism that may influence the attenuation of surface waves in a wave-ice field (Herman 2018, Herman et al. 2019, Marchenko et al. 2019b). An example of a splashing event is shown in Fig. 14. Some energy may also have dissipated in the towline and ice screws. None of the above-mentioned mechanisms were measured, only observed, and are therefore not quantified in this work.

In the present study, the ice concentration c_{ice} in the pool was 0.5, and the TKE dissipation rate was estimated in the range 0.057-0.92 Wm^{-2}. Voermans et al. (2019) estimated the dissipation rate of TKE per square meter surface area within the wave boundary layer (WBL) with the formula $D_{WBL} = \rho_w b_2(\pi H/T)^3$, where H is the wave height, T is the wave period and b_2 is a coefficient that can be interpreted as the ratio of TKE dissipation rate to the kinetic energy of the local wave state. The estimates were performed to describe wave damping in the MIZ of the Beaufort and Chukchi Seas due to the turbulence generated by waves and sea ice. They suggested that $b_2 = 10^{-7}e^{20c_{ice}}$, where $c_{ice} > 0.4$. Assuming $H = 0.2$ m and $T = 10$ s, we find $D_{WBL} = 0.0005\ \mathrm{Wm}^{-2}$ with $c_{ice} = 0.5$. The high value of the TKE dissipation rate in the present study compared to the values estimated with the formula by Voermans et al. (2019), is explained by the artificial excitation of the floe motion by winches. Our experiments were used for the estimates of relative energy portions spent for the generation of turbulence and collisions, and relative inputs of drag forces and collisions into the generation of turbulence. The estimations would have been less precise with lower TKE dissipation rates.

A discussion on the necessity of conducting full-scale tests in the field as opposed to laboratory experiments follows next. The dimensionless parameters of the investigated problem and their approximate values are listed in Table 7. In a laboratory experiment, it would be possible to obtain similarity by the Reynolds number, the Stokes number, the Poisson's ratio and the geometrical parameter H_f/L_f. However, it would be challenging to preserve the dimensionless groups Re/Fr and E/σ (Ashton 1986). The structure of natural ice influencing E and σ is determined by vertical profiles of ice temperature, salinity and porosity, which are usually not reproduced in model ice. The surface roughness

Dimensionless parameters	Formula	Value
Reynolds number	$Re = H_f v_f / \nu_w$	$\sim 5 \times 10^4$
Stokes number	$St = \rho_f / (\rho_w C)$	~ 1
Froude number	$Fr = v_f / \sqrt{g H_f}$	$\sim 3 \times 10^{-2}$
Cauchy number	$Ca = \rho_w v_f^2 / E$	$\sim 10^{-8}$
Poisson's ratio of ice	ν	$\sim 3 \times 10^{-1}$
	E/σ	$\sim 10^3$
dimension parameter	H_f / L_f	$1/4$
roughness parameter	r_f / H_f	$\sim 10^{-1}$
dimensionless B-V frequency	$N^2 H_f / g$	$\sim 4.5 \times 10^{-6}$
Richardson number	$Ri = N^2 / (dv_x/dz)^2$	$\sim 4.5 \times 10^{-3}$

Table 7: List of non-dimensional parameters of the problem and their approximate values, where H_f and L_f are the ice floe thickness and length, respectively, v_f is the representative floe velocity, ν_w is the kinematic viscosity of water, ρ_f and ρ_w are the densities of ice and water, respectively, $C \sim 1$ is the drag coefficient, g is the gravitational acceleration, $E \sim 1\text{GPa}$ and $\sigma \sim 1\text{MPa}$ are the elastic modulus and compression strength of ice, respectively, $r_f \sim 10^{-1}\text{m}$ is the roughness length of the submerged surface of the floe, $N \sim 6.7 \times 10^{-3}\text{s}^{-1}$ is the Brunt-Vaisala frequency and $dv_x/dz \sim 10^{-1}\text{s}^{-1}$ is the vertical gradient of the horizontal water velocity.

r_f of interacting floes is important for the process of floe-floe collisions, which causes the transformation of kinetic energy of the interacting floes into the energy of elastic waves in the ice and energy of viscous and anelastic deformations of the ice (Joseph et al. 2001). In full-scale tests, r_f changes in time due to thermodynamic processes and mechanical interaction of floes, which is very difficult to reproduce in laboratory experiments. Vertical profiles of water temperature and salinity below the ice influence the Richardson number and shear instability below drift ice through pressure effects. Water mixing below the ice caused by stratification is usually ignored in model tests, although the mixing is important for floe-floe interactions when the ice stresses are small. In cold weather, the atmosphere cooling causes water freezing in gaps between ice floes and slush production increases the effective viscosity of water around floes (de Carolis et al. 2005). This process is usually not reproduced in laboratory facilities. In fact, the relatively high air and ice temperatures that are maintained in laboratories to prevent fast growth of ice influence E, σ, r_f and slush production. All the above-mentioned effects confirm the importance of full-scale tests for the estimates of energy dissipation caused by floe-floe interactions in sea ice. In addition, the limited dimensions of a water tank may influence residual water currents and ice floe motion in a laboratory experiment.

6 Conclusions

Various mechanisms of energy dissipation and floe dynamics around a colliding full-scale ice floe have been investigated experimentally in an Arctic environment, and the paper presents much needed direct turbulence measurements. Relative water-ice motion was induced by towing the floe in an artificially made pool in the fast ice, back and forth in an oscillatory manner so that collisions with the fast ice occurred. The features of the constructed setup are similar to some processes that may occur in a dense field of small-sized ice floes when acted upon by long period ocean swell typically found in the MIZ. Extensive instrumentation, i.e., a load cell, a range meter, accelerometers, an IMU, an ADV, a high-resolution ADCP and an ROV, allowed for detailed surveillance of the towing load, floe motion and kinematics of the surrounding water. The average rate of input energy to the system, found from the towing load and the floe translational velocity in the axial direction, was 32.2 W.

Turbulence was generated from the relative water-ice velocity, comprising turbulent friction on the underside of the ice and the wake behind the floe, and from the downward water jets and upward suction motion associated with the collision events. The latter phenomenon was visualized with a new technique with rising bubbles and an ROV as tracers and camera, respectively. The large dispersion of the estimated TKE dissipation rate as a function of the ADCP location shows that the turbulent flow was not homogeneous. Turbulent kinetic energy frequency spectra were found to contain an inertial subrange where energy was cascading at a rate proportional to $f^{-5/3}$, according to Kolmogorov's theory. From spectral analysis, the total TKE rate due to the floe motion was estimated to be 11.9 W $\pm$64.6%, which corresponds to 36.9% $\pm$23.7% of the input energy rate. The dominating mechanism for wave energy dissipation in ice floe fields is still debated. Despite of uncertainties, these results indicate that a substantial portion of the attenuated wave energy may be dissipated in turbulence. From the accelerometer data, energy absorption due to collisions was calculated as the change in the kinetic energy of the floe immediately before and after the collision events. The estimated rate of energy loss in this process was 2.4 W, i.e., 7.5% of the input energy rate, which was attributed to elastic ice deformation and slush production.

Acknowledgments

This study was supported by the Research Council of Norway under the PETROMAKS2 scheme (DOFI, Grant number 28062) and the IntPart project Arctic Offshore and Coastal Engineering in Changing Climate (Project number 274951). The authors are grateful to Andrej Sliusarenko, Vladimir Markov and Sergej Podleshych for their assistance. We also thank Olav Gundersen for the winch setup and Store Norske for accommodating the researcher in Svea while performing the experiments.

Author declarations

The authors have no conflicts to disclose.

Data availability

The data that support the findings of this study are available from the corresponding author upon reasonable request.

A Instrument synchronization

It was necessary to synchronize the range meter and load cell time series in the post processing in order to calculate the winch power applied on the ice floe. The synchronization scheme described herein applies for the instruments marked with diamonds in Table 2. As mentioned in Sec. 2.1, the range meter was sampled in correct UTC time in the first place. The load cell and the accelerometers were connected to the same data acquisition unit and therefore synchronized, but the computer clock was incorrect. The data were first re-sampled to a common sampling rate of 1 kHz. From the uniaxial accelerometer time series, distinct peaks were recognized at the instance of impact, as elaborated in Sec. 4.2. The IMU, which sampled in correct GPS time, produced the same peaks in the time series. Hence, the correct UTC time of the first impact in Exp. 3 was found from the IMU time series. Finally, the acceleration and load cell time series were shifted to coincide with this instance.

B Ice floe kinetic energy

The kinetic energy of surge motion of the ice floe $K_{s,0}$, where the added mass effect is neglected, is $K_{s,0} = mv_{f,x}^2/2$. From Fig. 6, it is clear that the surge velocity is a periodic function with amplitude V_{max} and period T_s, so $v_{f,x}$ is approximated as $v_{f,x} \approx V_{max}\sin(\omega_s t)$, where $\omega_s = 2\pi/T_s$ is the angular frequency of the surge motion and t is the time. The mean kinetic energy of surge motion averaged over the surge period is estimated as

$$\langle K_{s,0}\rangle \approx \frac{\int_0^{T_s} mV_{max}^2 \sin^2(\omega_s t)dt}{2T_s} = 60.8 \text{ J}, \tag{B1}$$

where the values $m = 10800$ kg, $V_{max} = 0.15 \text{ ms}^{-1}$ and $T_s = 26$ s are inserted. When the added mass is included, the kinetic energy of surge motion is K_s, where $K_s > K_{s,0}$. However, the difference between K_s and $K_{s,0}$ is assumed to be small since the added mass in the axial direction is small compared to the floe mass. The average power of the surge motion P_s is approximated as $P_s \approx \langle K_{s,0}\rangle/T_s = 2.3$ W.

In Sec. 2.1, it was stated that the motion in the vertical modes was negligible compared with the horizontal modes. This is illustrated in Fig. 15, where the surge amplitudes are much greater than the heave amplitudes. Note that the surge periods T_s are around 26 s and the heave periods T_h are around 2 s, which agrees with the uniaxial accelerometers in the lower panel of Fig. 3 and the frequency of natural oscillations in the vertical direction f_h that was theoretically estimated in Sec. 5. The heave amplitudes A_h are in the order of 1 cm. The mean kinetic energy of heave motion averaged over the heave period is estimated as

$$E_h \approx m\left(1 + \frac{m_{ad}}{m}\right)\frac{(\omega_h A_h)^2}{4} = 3.0 \text{ J}, \tag{B2}$$

where the values $m = 10800$ kg, $m_{ad} = 2955$ kg (added mass in the vertical direction), $\omega_h = 2\pi f_h = 2.95 \text{ rads}^{-1}$ (angular frequency of the surge motion) and $A_h = 1 \text{ cm}$ are inserted. The average power of the heave motion P_h is approximated as $P_h \approx E_h/T_s = 0.1$ W.

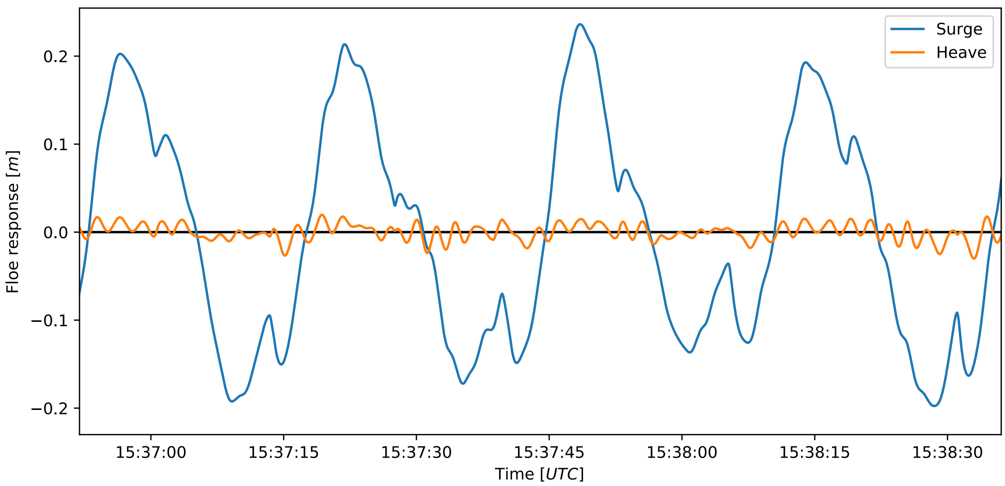

Figure 15: Surge and heave response of the ice floe in Exp. 3.

References

Arote, A., Bade, M. & Banerjee, J. (2020), 'On coherent structures of spatially oscillating planar liquid jet developing in a quiescent atmosphere', *Physics of Fluids* **32**(8), 082111.

Ashton, G. D. (1986), *River and lake ice engineering*, Water Resources Publication, Colorado.

Baudry, V., Babarit, A. & Clement, A. (2013), An overview of analytical, numerical and experimental methods for modelling oscillating water columns, *in* 'EWTEC'.

Bertuccioli, L., Roth, G. I., Katz, J. & Osborn, T. R. (1999), 'A submersible particle image velocimetry system for turbulence measurements in the bottom boundary layer', *Journal of Atmospheric and Oceanic Technology* **16**(11), 1635–1646.

BlueRobotics (2020), 'Bluerov2'.
URL: *https://bluerobotics.com/store/rov/bluerov2/*

Breda, M. & Buxton, O. R. (2018), 'Influence of coherent structures on the evolution of an axisymmetric turbulent jet', *Physics of Fluids* **30**(3), 035109.

Cafiero, G. & Vassilicos, J. (2019), 'Non-equilibrium turbulence scalings and self-similarity in turbulent planar jets', *Proceedings of the royal society A* **475**(2225), 20190038.

de Carolis, G., Olla, P. & Pignagnoli, L. (2005), 'Effective viscosity of grease ice in linearized gravity waves', *Journal of Fluid Mechanics* **535**, 369–381.

Dewey, R. & Stringer, S. (2007), 'Reynolds stresses and turbulent kinetic energy estimates from various adcp beam configurations: Theory', *J. of Phys. Ocean* pp. 1–35.

Dugan, J., DiMarco, R. & Martin, W. (1992), 'Low-frequency vibrational motion of arctic pack ice', *Journal of Geophysical Research: Oceans* **97**(C4), 5381–5388.

Earle, M. D. (1996), ‘Nondirectional and directional wave data analysis procedures’, *NDBC Tech. Doc* **96**(002).

Feltham, D. (2015), ‘Arctic sea ice reduction: the evidence, models and impacts’, *Philosophical Transactions of the Royal Society of London A: Mathematical, Physical and Engineering Sciences* **373**(2045).

Greene, A., Hendricks, P. & Gregg, M. (2015), ‘Using an adcp to estimate turbulent kinetic energy dissipation rate in sheltered coastal waters’, *Journal of Atmospheric and Oceanic Technology* **32**(2), 318–333.

Guerra, M. & Thomson, J. (2017), ‘Turbulence measurements from five-beam acoustic doppler current profilers’, *Journal of Atmospheric and Oceanic Technology* **34**(6), 1267–1284.

Herman, A. (2018), ‘Wave-induced surge motion and collisions of sea ice floes: Finite-floe-size effects’, *Journal of Geophysical Research: Oceans* **123**(10), 7472–7494.

Herman, A. (2021), ‘Spectral wave energy dissipation due to under-ice turbulence’, *Journal of Physical Oceanography* **51**(4), 1177–1186.

Herman, A., Cheng, S. & Shen, H. H. (2019), ‘Wave energy attenuation in fields of colliding ice floes–part 2: A laboratory case study’, *The Cryosphere* **13**(11), 2901–2914.

Herman, A., Evers, K.-U. & Reimer, N. (2018), ‘Floe-size distributions in laboratory ice broken by waves’, *The Cryosphere* **12**(2), 685–699.

Hertz, H. (1882), ‘On the contact of rigid elastic solids and on hardness, chapter 6: Assorted papers by h. hertz’.

Joseph, G., Zenit, R., Hunt, M. & Rosenwinkel, A. (2001), ‘Particle-wall collisions in a viscous fluid’, *Journal of Fluid Mechanics* **433**, 329–346.

Kohout, A. L., Meylan, M. H. & Plew, D. R. (2011), ‘Wave attenuation in a marginal ice zone due to the bottom roughness of ice floes’, *Annals of Glaciology* **52**(57), 118–122.

Kolaas, J. (2016), ‘Getting started with hydrolabpiv v1. 0’, *Research report in mechanics http://urn. nb. no/URN: NBN: no-23419* .

Kolmogorov, A. N. (1941), ‘The local structure of turbulence in incompressible viscous fluid for very large reynolds numbers’, *Doklady Akademiia Nauk SSSR* **30**, 301–305.

Landau, L. D. & Lifshitz, E. M. (1987*a*), *Course of theoretical physics: Fluid Mechanics*, Vol. 6, Pergamon Press.

Landau, L. D. & Lifshitz, E. M. (1987*b*), *Course of theoretical physics: Theory of Elasticity*, Vol. 7, Pergamon Press.

Layek, G. & Sunita (2018), ‘Non-kolmogorov scaling and dissipation laws in planar turbulent plume’, *Physics of Fluids* **30**(11), 115105.

Li, H. & Lubbad, R. (2018), Laboratory study of ice floes collisions under wave action, *in* ‘The 28th International Ocean and Polar Engineering Conference’, International Society of Offshore and Polar Engineers (ISOPE).

Liu, A. K. & Mollo-Christensen, E. (1988), ‘Wave propagation in a solid ice pack’, *Journal of physical oceanography* **18**(11), 1702–1712.

Løken, T. K., Ellevold, T. J., de la Torre, R. G. R., Rabault, J. & Jensen, A. (2021a), ‘Bringing optical fluid motion analysis to the field: a methodology using an open source rov as camera system and rising bubbles as tracers’, *Measurement Science and Technology* **32**(9).

Løken, T. K., Marchenko, A., Ellevold, T. J., Rabault, J. & Jensen, A. (2021b), An investigation into the turbulence induced by moving ice floes, *in* 'Proc. of the 26th International Conference on Port and Ocean Engineering under Arctic Conditions (POAC 2021)', Springer, Moscow, Russia.

Lu, Y. & Lueck, R. G. (1999), 'Using a broadband adcp in a tidal channel. part ii: Turbulence', *Journal of Atmospheric and Oceanic Technology* **16**(11), 1568–1579.

Lumley, J. & Terray, E. (1983), 'Kinematics of turbulence convected by a random wave field', *Journal of Physical Oceanography* **13**(11), 2000–2007.

Marchenko, A., Chistyakov, P. V., Karulin, E. B., Markov, V. V., Morozov, E. G., Karulina, M. M. & Sakharov, A. N. (2021a), Field experiments on collisional interaction of floating ice blocks, *in* 'Proc. of the 26th International Conference on Port and Ocean Engineering under Arctic Conditions (POAC 2021)', Springer, Moscow, Russia.

Marchenko, A., Gorbatsky, V. & Turnbull, I. (2015), Characteristics of under-ice ocean currents measured during wave propagation events in the barents sea, *in* 'Proceedings of the International Conference on Port and Ocean Engineering Under Arctic Conditions'.

Marchenko, A., Grue, J., Karulin, E., Frederking, R., Lishman, B., Chistyakov, P., Karulina, M., Sodhi, D., Renshaw, C., Sakharov, A. et al. (2020), Elastic moduli of sea ice and lake ice calculated from in-situ and laboratory experiments, *in* '25th IAHR International Symposium on Ice', The International Association for Hydro-Environment Engineering and Research.

Marchenko, A., Haase, A., Jensen, A., Lishman, B., Rabault, J., Evers, K.-U., Shortt, M. & Thiel, T. (2021), 'Laboratory investigations of the bending rheology of floating saline ice and physical mechanisms of wave damping in the hsva hamburg ship model basin ice tank', *Water* **13**(8), 1080.

Marchenko, A., Karulin, E. & Chystiakov, P. (2021b), Experimental investigation of viscous-elastic properties of columnar sea ice, *in* 'Proc. of the 26th International Conference on Port and Ocean Engineering under Arctic Conditions (POAC 2021)', Springer, Moscow, Russia.

Marchenko, A., Markov, V. & Taylor, R. (2019b), Influence of water on collisions of floating ice blocks, *in* 'The 29th International Ocean and Polar Engineering Conference', International Society of Offshore and Polar Engineers.

Marchenko, A., Wadhams, P., Collins, C., Rabault, J. & Chumakov, M. (2019a), 'Wave-ice interaction in the north-west barents sea', *Applied Ocean Research* **90**, 101861.

Marsan, D., Weiss, J., Moreau, L., Gimbert, F., Doble, M., Larose, E. & Grangeon, J. (2019), 'Characterizing horizontally-polarized shear and infragravity vibrational modes in the arctic sea ice cover using correlation methods', *The Journal of the Acoustical Society of America* **145**(3), 1600–1608.

Martin, S. & Becker, P. (1987), 'High-frequency ice floe collisions in the greenland sea during the 1984 marginal ice zone experiment', *Journal of Geophysical Research: Oceans* **92**(C7), 7071–7084.

Martin, S. & Becker, P. (1988), 'Ice floe collisions and their relation to ice deformation in the bering sea during february 1983', *Journal of Geophysical Research: Oceans* **93**(C2), 1303–1315.

McKenna, R. F. & Crocker, G. B. (1992), 'Ice-floe collisions interpreted from acceleration data during limex '89', *Atmosphere-Ocean* **30**(2), 246–269.

Nystrom, E. A., Rehmann, C. R. & Oberg, K. A. (2007), 'Evaluation of mean velocity and turbulence measurements with adcps', *Journal of hydraulic engineering* **133**(12), 1310–1318.

Rabault, J., Sutherland, G., Gundersen, O., Jensen, A., Marchenko, A. & Breivik, Ø. (2020), 'An open source, versatile, affordable waves in ice instrument for scientific measurements in the polar regions', *Cold Regions Science and Technology* **170**, 102955.

Rabault, J., Sutherland, G., Jensen, A., Christensen, K. H. & Marchenko, A. (2019), 'Experiments on wave propagation in grease ice: combined wave gauges and particle image velocimetry measurements', *Journal of Fluid Mechanics* **864**, 876–898.

Rottier, P. J. (1992), 'Floe pair interaction event rates in the marginal ice zone', *Journal of Geophysical Research: Oceans* **97**(C6), 9391–9400.

Shen, H. H. (2019), 'Modelling ocean waves in ice-covered seas', *Applied Ocean Research* **83**, 30–36.

Shen, H. H. & Ackley, S. F. (1991), 'A one-dimensional model for wave-induced ice-floe collisions', *Annals of Glaciology* **15**, 87–95.

Shen, H. H. & Squire, V. A. (1998), 'Wave damping in compact pancake ice fields due to interactions between pancakes', *Antarctic Sea Ice: Physical Processes, Interactions and Variability* **74**, 325–341.

Smith, L. C. & Stephenson, S. R. (2013), 'New trans-arctic shipping routes navigable by midcentury', *Proceedings of the National Academy of Sciences* **110**(13), E1191–E1195.

Smith, M. & Thomson, J. (2019), 'Ocean surface turbulence in newly formed marginal ice zones', *Journal of Geophysical Research: Oceans* **124**(3), 1382–1398.

Smith, M. & Thomson, J. (2020), 'Pancake sea ice kinematics and dynamics using shipboard stereo video', *Annals of Glaciology* **61**(82), 1–11.

Smith, W. N., Atsavapranee, P., Katz, J. & Osborn, T. (2002), 'Piv measurements in the bottom boundary layer of the coastal ocean', *Experiments in Fluids* **33**(6), 962–971.

Spiegel, M. R. & Liu, J. (1999), *Mathematical handbook of formulas and tables*, McGraw-Hill.

Squire, V. A., Dugan, J. P., Wadhams, P., Rottier, P. J. & Liu, A. K. (1995), 'Of ocean waves and sea ice', *Annual Review of Fluid Mechanics* **27**(1), 115–168.

Sreenivasan, K. R. (1995), 'On the universality of the kolmogorov constant', *Physics of Fluids* **7**(11), 2778–2784.

Sutherland, G. & Rabault, J. (2016), 'Observations of wave dispersion and attenuation in landfast ice', *Journal of Geophysical Research: Oceans* **121**(3), 1984–1997.

Sutherland, G., Rabault, J., Christensen, K. H. & Jensen, A. (2019), 'A two layer model for wave dissipation in sea ice', *Applied Ocean Research* **88**, 111–118.

Takahashi, M., Iwano, K., Sakai, Y. & Ito, Y. (2019), 'Three-dimensional visualization of destruction events of turbulent momentum transfer in a plane jet', *Physics of Fluids* **31**(10), 105114.

Tennekes, H. (1975), 'Eulerian and lagrangian time microscales in isotropic turbulence', *Journal of Fluid Mechanics* **67**(3), 561–567.

Thomson, J., Polagye, B., Durgesh, V. & Richmond, M. C. (2012), 'Measurements of turbulence at two tidal energy sites in puget sound, wa', *IEEE Journal of Oceanic Engineering* **37**(3), 363–374.

Thomson, J. & Rogers, W. E. (2014), 'Swell and sea in the emerging arctic ocean', *Geophysical Research Letters* **41**(9), 3136–3140.

Timco, G. & Weeks, W. (2010), 'A review of the engineering properties of sea ice', *Cold regions science and technology* **60**(2), 107–129.

TopoSvalbard, N. P. I. (2021), 'Topological map'.
URL: *https://toposvalbard.npolar.no/*

Variano, E. A. & Cowen, E. A. (2008), 'A random-jet-stirred turbulence tank', *Journal of Fluid Mechanics* **604**, 1–32.

Voermans, J., Babanin, A., Thomson, J., Smith, M. & Shen, H. (2019), 'Wave attenuation by sea ice turbulence', *Geophysical Research Letters* **46**(12), 6796–6803.

Voulgaris, G. & Trowbridge, J. H. (1998), 'Evaluation of the acoustic doppler velocimeter (adv) for turbulence measurements', *Journal of atmospheric and oceanic technology* **15**(1), 272–289.

Wadhams, P. (1975), 'Airborne laser profiling of swell in an open ice field', *Journal of Geophysical Research* **80**(33), 4520–4528.

Wadhams, P., Squire, V. A., Goodman, D. J., Cowan, A. M. & Moore, S. C. (1988), 'The attenuation rates of ocean waves in the marginal ice zone', *Journal of Geophysical Research: Oceans* **93**(C6), 6799–6818.

Weber, J. E. (1987), 'Wave attenuation and wave drift in the marginal ice zone', *Journal of physical oceanography* **17**(12), 2351–2361.

Zhao, X. & Shen, H. H. (2018), 'Three-layer viscoelastic model with eddy viscosity effect for flexural-gravity wave propagation through ice cover', *Ocean Modelling* **131**, 15–23.

Zippel, S. F., Thomson, J. & Farquharson, G. (2018), 'Turbulence from breaking surface waves at a river mouth', *Journal of Physical Oceanography* **48**(2), 435–453.